AGU PUBLICATIONS

JGR

Journal of Geophysical Research: Oceans

RESEARCH ARTICLE

10.1002/2014JC010557

Key Points:
- Numeric Lagrangian pathways to the North Atlantic OMZ are computed
- Transfer of mass from the subtropical gyre to the shadow zone appears in the ICW
- A 50% contribution of NACW makes up the core of the North Atlantic OMZ

Supporting Information:
- Supporting Information S1
- Movie S1

Correspondence to:
J. Peña-Izquierdo,
susope@icm.csic.es

Citation:
Peña-Izquierdo, J., E. van Sebille, J. L. Pelegrí, J. Sprintall, E. Mason, P. J. Llanillo, and F. Machín (2015), Water mass pathways to the North Atlantic oxygen minimum zone, *J. Geophys. Res. Oceans*, *120*, 3350–3372, doi:10.1002/2014JC010557.

Received 5 NOV 2014
Accepted 30 MAR 2015
Accepted article online 3 APR 2015
Published online 8 MAY 2015

Water mass pathways to the North Atlantic oxygen minimum zone

Jesús Peña-Izquierdo[1], Erik van Sebille[2,3], Josep L. Pelegrí[1], Janet Sprintall[4], Evan Mason[5], Pedro J. Llanillo[1,6], and Francisco Machín[7]

[1]Departament d'Oceanografia Física i Tecnológica, Institut de Ciències del Mar, ICM-CSIC, Barcelona, Spain, [2]Climate Change Research Centre and ARC Centre of Excellence for Climate System Science, University of New South Wales, Sydney, NSW, Australia, [3]Now at Department of Physics, Grantham Institute, Imperial College, London, UK, [4]Climate, Atmospheric Sciences, and Physical Oceanography Department, Scripps Institution of Oceanography, University of California, La Jolla, San Diego, California, USA, [5]Instituto Mediterráneo de Estudios Avanzados, IMEDEA-CSIC, Esporles, Spain, [6]Now at Departmento de Física, Universidad de Santiago de Chile, Santiago, Chile, [7]InvestigAdHoc S.A., Telde, Spain

Abstract The water mass pathways to the North Atlantic Oxygen Minimum Zone (naOMZ) are traditionally sketched within the cyclonic tropical circulation via the poleward branching from the eastward flowing jets that lie south of 10°N. However, our water mass analysis of historic hydrographic observations together with numerical Lagrangian experiments consistently reveal that the potential density level of $\sigma_\theta = 26.8$ kg m^{-3} (σ26.8, approximately 300 m depth) separates two distinct regimes of circulation within the Central Water (CW) stratum of the naOMZ. In the upper CW (above σ26.8), and in agreement with previous studies, the supply of water mainly comes from the south with a predominant contribution of South Atlantic CW. In the lower CW (below σ26.8), where minimal oxygen content is found, the tropical pathway is instead drastically weakened in favor of a subtropical pathway. More than two thirds of the total water supply to this lower layer takes place north of 10°N, mainly via an eastward flow at 14°N and northern recirculations from the northern subtropical gyre. The existence of these northern jets explains the greater contribution of North Atlantic CW observed in the lower CW, making up to 50% of the water mass at the naOMZ core. The equatorward transfer of mass from the well-ventilated northern subtropical gyre emerges as an essential part of the ventilation of the naOMZ.

1. Introduction

The classical theory on thermocline ventilation [*Luyten et al.*, 1983] postulates the existence of regions at the eastern margin of the ocean isolated from the wind-driven circulation. A sluggish circulation characterizes these so-called shadow zones that are located between the well-ventilated subtropical gyres and the tropical system of zonal jets. In addition to the weak ventilation, the microbial respiration of the organic matter from the nearby highly productive coastal upwelling system leads to the development of oxygen minimum zones (OMZs) between 100 and 900 m depths, thus within Central Water (CW) and Intermediate Water (IW) strata [*Karstensen et al.*, 2008].

All OMZs present hypoxic conditions under which most marine species cannot survive [*Vaquer-Sunyer and Duarte*, 2008]. Moreover, oxygen also plays an essential role in biogeochemical processes, such as in the nitrogen and carbon cycles [*Bopp et al.*, 2002; *Lam and Kuypers*, 2011; *Paulmier et al.*, 2011], with a direct impact on climate dynamics. Several decades of observations have revealed that the world ocean OMZs are, on average, growing and reducing their oxygen content [*Garcia et al.*, 1998; *Joos et al.*, 2003; *Stramma et al.*, 2008a, 2009]. This trend has been related to global warming and increased CO_2 levels [*Matear and Hirst*, 2003; *Oschlies et al.*, 2008], as well as to natural decadal variability [*Gnanadesikan et al.*, 2007; *Deutsch et al.*, 2011], but the exact ways how this is happening are yet to be deciphered. The key role of oxygen content for the marine ecosystem endorses the crucial need for a better understanding of the OMZs dynamics.

In this study we will focus on the North Atlantic OMZ (naOMZ) and how its water mass is renewed. Earlier studies have assumed that most of the water supply to the naOMZ comes from the south, through the cyclonic tropical circulation pattern [*Stramma et al.*, 2005, 2008b; *Brandt et al.*, 2010, 2014], in agreement with the idea of a shadow zone in the subtropical gyre [*Luyten et al.*, 1983] where the Cape Verde frontal

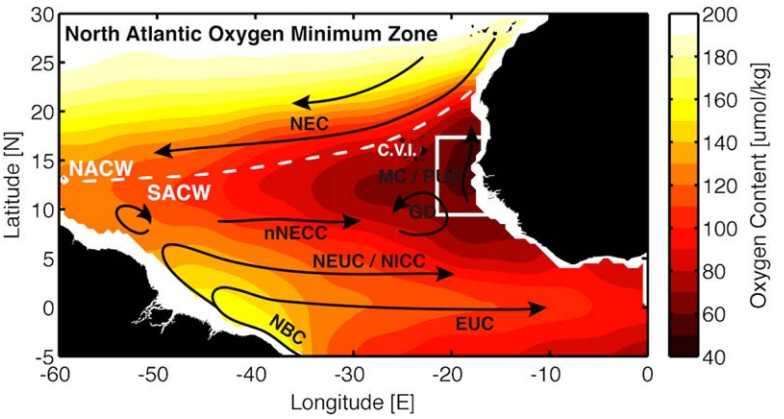

Figure 1. Schematic circulation pattern in the tropical Atlantic Ocean as derived from previous studies, overlying the climatological oxygen content of the 200–500 m layer. The naOMZ box (Lagrangian particles release region) is indicated by a white box. The frontal zone between SACW and NACW is shown as a white-dashed line; C.V.I. refers to the Cape Verde Islands. Main currents: North Brazil Current (NBC), Equatorial Undercurrent (EUC), North Equatorial Undercurrent (NEUC), North Intermediate Countercurrent (NICC), northern branch of the North Equatorial Countercurrent (nNECC), Mauritanian Current (MC), Poleward Undercurrent (PUC), Guinea Dome (GD), and North Equatorial Current (NEC).

region acts as the barrier between the subtropical and the tropical gyres [*Fraga*, 1974; *Zenk et al*., 1991]. The existence of an interhemispheric northward transfer of mass linked to the upper limb of the Atlantic Meridional Overturning Circulation further leads to the predominance of southern origin waters in the whole tropical thermocline [*Kirchner et al*., 2009]. South Atlantic CW (SACW) and Antarctic IW (AAIW) cross the equator mostly along the western margin via the North Brazil Current (NBC) and partly retroflect east to feed the tropical system of jets (Figure 1). The considered major pathways to the naOMZ are therefore subsurface eastward jets located south of 10°N: the North Intermediate CounterCurrent (NICC) at 2°N, the North Equatorial Undercurrent (NEUC) at 4°N, and the northern branch of the North Equatorial Countercurrent (nNECC) at 8°N–9°N [*Stramma et al*., 2005; *Karstensen et al*., 2008; *Brandt et al*., 2010]. Nevertheless, the core of the naOMZ lies further north. The link between these jets and the naOMZ is therefore explained by the cyclonic circulation around the Guinea Dome, a general uplift of the isopycnals within the surface and subsurface levels driven by the local cyclonic wind stress [*Siedler et al*., 1992; *Lázaro et al*., 2005]. Moreover, this northward branching to the naOMZ is enhanced along the African continent by the seasonal Mauritanian Current at the surface and by the ubiquitous subsurface along-slope Poleward Undercurrent [*Barton*, 1989; *Mittelstaedt*, 1991; *Peña-Izquierdo et al*., 2012].

In addition to the advective supply, recent observational studies point out the notable role that meridional mesoscale stirring [*Hahn et al*., 2014] and diapycnal diffusion [*Fischer et al*., 2013] play in the local renewal of the naOMZ thermocline. These processes are especially relevant in the oxygen supply to the naOMZ, because of the strong meridional gradients in the oxygen field, which are related to the predominant zonal circulation. However, it is the large-scale circulation that is the primary factor in settling the development of the naOMZ, while mixing leads to a homogenization of the hydrographic properties within. In this sense, while direct velocity and Lagrangian drifters show a clear connection between the NEUC/nNECC and the naOMZ at depths above 300 m [*Stramma et al*., 2005, 2008b; *Brandt et al*., 2010], neither observations nor numerical simulations [*Elmoussaoui et al*., 2005] give evidence for a link at deeper levels. We may, therefore, wonder what is the maximum depth reached by this circulation scheme and what are the responsible dynamics further below.

Some hints to a vertical limit in the connection between the NEUC/nNECC and the naOMZ come from historical temperature and salinity profiles in the eastern tropical North Atlantic. A salinity and temperature inversion is usually observed at $\sigma_\theta = 26.8$ kg m^{-3} (σ26.8), located at about 300 m within the CW stratum [*Fraga*, 1974; *Voituriez and Chuchla*, 1978; *Poole and Tomczak*, 1999; *Pastor et al*., 2012; *Peña-Izquierdo et al*., 2012]. Fresher and colder waters are only found above this level, indicative of SACW, while an enhanced influence of saltier and warmer North Atlantic CW (NACW) is present below. *Voituriez and Chuchla* [1978] earlier proposed that this thermohaline transition at σ26.8 corresponds to a mean northward penetration of SACW in the overlying layer and a southward inflow of NACW in the underlying layer. Nevertheless, the circulation pattern leading to such a transition has not yet been properly addressed.

The numerical simulation of *Elmoussaoui et al*. [2005] shows that σ26.8 roughly matches with the deepest vertical extent of the northward branch of the nNECC heading toward the naOMZ. Their results suggest that no direct water supply associated with the NEUC/nNECC, and in turn with SACW, takes place below this level. Indeed, oxygen concentrations decrease rapidly in the naOMZ below σ26.8 [*Fischer et al*., 2013], pointing to a weaker ventilation. The signal of NACW in this deep layer is especially relevant because (1) it points to a new pathway and source of oxygen for the naOMZ, not previously taken into account, and (2) reveals a vertical limit to the constraint for the equatorward transfer of mass from the subtropical gyre to the shadow zone [*Luyten et al*., 1983].

While other studies on the ventilation of OMZs have focused on the role played by the tropical system of jets, in this study we investigate all the sources to the naOMZ CWs, with particular emphasis on the northern subtropical gyre contribution. In order to determine the geographical and vertical distribution of SACW and NACW, we first carry out a water mass analysis for the whole tropical Atlantic from historical observations. We then perform a numerical Lagrangian experiment to compute the water mass pathways toward the naOMZ. The Lagrangian approach allows us to consider the combined effect of mean flow, seasonal variability, and mesoscale eddies—incorporating the regional and mesoscale diapycnal advection—which have been considered separately in earlier observational studies [*Stramma et al*., 2005, 2008b; *Brandt et al*., 2010; *Hahn et al*., 2014]. The joint analysis of the water mass distribution, as deduced from observations, and the water mass composition, as deduced from the Lagrangian pathways, provides independent but consistent views of the principal processes leading to water mass renewal of the naOMZ.

2. Data and Methods

2.1. Data Set of T/S Profiles

This work focuses on the northeastern tropical Atlantic Ocean but, as we are interested in the origin of the naOMZ water mass, the area of study spans the entire North Atlantic tropical Ocean (from 60°W to 0°E) and from the southern hemisphere to beyond the southern edge of the North Atlantic Subtropical Gyre (from 5°S to 30°N). A data set of observed temperature and salinity (*T/S*) profiles has been used, instead of a climatological database, to avoid the loss of variability after climatologic averaging. This data set has been created with CTD profiles obtained from the National Oceanographic Data Center (http://www.nodc.noaa.gov) together with Argo profiles downloaded from the European Argo Data Center (http://www.coriolis.eu.org). While the set of CTD profiles used here spans a longer period of time (since 1971), they are fewer than the number of available Argo profiles, which has been growing fast since 2005. Both Argo real time and delayed mode profiles have been included in this data set. The initial data set includes 21,242 CTD casts and 39,919 Argo profiles, comprising data from 1971 to 2011. All *T/S* profiles are converted to the TEOS-10 formulation, i.e., conservative temperature and absolute salinity [*Millero et al*., 2008].

Although the data centers perform an automatic quality control on the data, an additional procedure has been followed to ensure we have a high-quality set of data: (1) for the CTD data set, only profiles with an "accepted" NODC quality flag are used; (2) for the Argo data set, only data with a "good" quality flag are selected; (3) profilers included in the gray list provided by the Argo data centers are removed; (4) all profiles are required to span the entire depth range between 100 and 1000 m to ensure the sampling of the upper thermocline, with a minimum vertical resolution of 10 m for the whole profile; (5) all profiles with density inversions greater than 0.01 kg m^{-3} are removed.

After this initial selection, we retain a total of 9607 CTD's and 30,136 Argo *T/S* profiles. The *T/S* values are then linearly interpolated to selected potential density levels, on average separated by about 10 m. These interpolated profiles are then sorted geographically in bins of 3.5° × 5° of latitude and longitude for a final statistical test. The average *T* and *S* values at each density level are computed for each bin so that any profile with data beyond three standard deviations from the mean is removed. The final (*T/S*) data set includes 30,485 profiles on σ_θ coordinates.

We also use the ocean oxygen content field from the annual WOCE atlas [*Gouretski and Koltermann*, 2004] with 0.5° horizontal resolution and 45 vertical levels. An advantageous feature of this climatology is the averaging on isopycnal levels, instead of the more common isobaric computation. This method mimics the preferential along-isopycnal mixing that occurs in the real ocean and therefore preserves the water mass

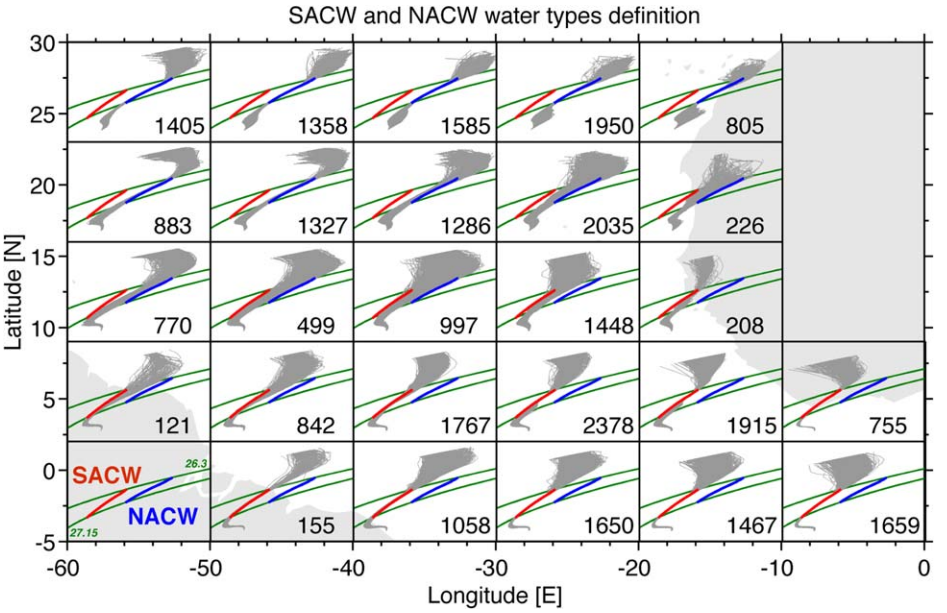

Figure 2. *T/S* diagrams for all available profiles inside each 10° latitude × 7° longitude bin. Each box shows the definition of SACW/NACW (red/blue lines), the isopycnal limits of the central water stratum (σ26.3–σ27.15, green lines), and the number of observational profiles.

identities. For this same reason, throughout the whole manuscript we will use potential density instead of depth coordinates.

2.2. Water Mass Analysis

A water mass analysis is carried out to distinguish the contribution of water masses with southern and northern origin to the naOMZ thermocline. We focus on the CW stratum where the upper part of the naOMZ is found; therefore, only the contributions of NACW and SACW are calculated. We define these two water types as the mean *T/S* profiles calculated between latitudes 5°S and 0°S for SACW, and between 25°N and 30°N for NACW, after averaging on isopycnal surfaces. The averaged profiles are computed within the CW stratum, defined in the tropical Atlantic Ocean for σ_θ between 26.3 and 27.15 kg m^{-3} [*Kirchner et al.*, 2009]. Figure 2 shows how these definitions of SACW and NACW correctly confine the variability of CWs within the tropical Atlantic.

The analysis here implemented is a simplified isopycnal version of the optimum multiparameter analysis [*Mackas et al.*, 1987; *Tomczak and Large*, 1989]. The method aims at finding the contribution of predefined water types to each data point, determined as the best linear mixing combination in a multivariable space. In our case we use only two hydrographic variables (temperature and salinity) together with the mass conservation constraint.

For every data point, each modeled variable $V_{Mod,i}$ (i.e., *T*, *S* and mass) is calculated from a combination of SACW and NACW proportions (x_{SACW} and x_{NACW})

$$V_{Mod,i} = x_{SACW} V_{SACW,i} + x_{NACW} V_{NACW,i},$$

where $V_{SACW,i}$ and $V_{NACW,i}$ denote the values of the normalized variable *i* for the SACW and NACW water types at the density of the observation. For the conservation of mass ($i = mass$), the above equation becomes simply $V_{Mod,mass} = x_{SACW} + x_{NACW}$.

The best combination is obtained minimizing, in a nonnegative least squares sense, the total residual *R*, defined as

$$R = \sum_{i=T,S,mass} w_i r_i \equiv \sum_{i=T,S,mass} w_i \left(V_{Mod,i} - V_{Obs,i}\right) = \sum_{i=T,S,mass} w_i \left[\left(x_{SACW} V_{SACW,i} + x_{NACW} V_{NACW,i}\right) - V_{Obs,i}\right].$$

This total residual represents the weighed summation of the residuals of all three variables (r_i), each one calculated as the difference between the modeled ($V_{Mod,i}$) and observed ($V_{Obs,i}$) values. While the *T* and *S*

residuals are weighted equally ($w_T = w_S = 1$), mass conservation is enforced through a much a greater weight ($w_{mass} = 10$), therefore ensuring that the water sample is almost totally made from the combination of the predefined water types; note that $V_{Obs,mass} = 1$.

2.3. The Velocity Field

The numerical simulation used in this study is the open access product from the ECCO2 project (Estimating the Circulation and Climate of the Ocean, phase II, http://ecco2.jpl.nasa.gov). The ECCO2 velocity fields are obtained by a least squares fit of the outputs of a global full-depth-ocean and sea-ice configuration of the Massachusetts Institute of Technology Ocean General Circulation Model [*Marshall et al*., 1997] to the available observations. It uses both satellite and in situ available data, including the CTD casts and Argo profiles described above. The simulation is an eddy-permitting solution with a 1/4° horizontal resolution and 50 vertical levels, spanning 20 years from 1992 to 2011 with a temporal resolution of 3 days. The model, therefore, is capable of reproducing the largest mesoscale features but cannot simulate the turbulence associated with scales smaller than 1/4°. A comparison between satellite altimeter and the ECCO2 velocity fields [*Fu*, 2009] shows good agreement in the latitudinal variation of surface zonal velocities, a reflection of the tropical system of zonal jets. A comparison between the water mass distribution as calculated from hydrographic observations and the water mass distribution deduced from the modeled Lagrangian pathways is discussed in section 4. In section 5, the velocity fields from several observational studies are also compared with the model velocity field.

We will use two different velocity fields to describe the processes that lead to the thermohaline transition at σ26.8. On a first and simplified case, we will use a fully isopycnal two-dimensional (2-D) field, computed by vertically averaging the original ECCO2 horizontal velocities over 0.05 kg m^{-3} potential density layers. The Lagrangian advection within this 2-D field will always follow isopycnal surfaces and the vertical velocity is therefore solely related to the isopycnals' slope. Second, we will use the original three-dimensional (3-D) ECCO2 velocity field. The comparison between both of these velocity fields will allow us to distinguish between the isopycnal and diapycnal components of the velocity in the ECCO2 product.

The vertical velocity field in ECCO2 does not capture small-scale processes like double diffusion or turbulence related to vertical shear instabilities. Hence, in this work only the contribution of regional scale and mesoscale diapycnal advection, as resolved by the model, are taken into account for estimating the diapycnal component of the naOMZ thermocline renewal (hereafter referred as diapycnal fluxes). We will take special caution when interpreting these results because the vertical velocity in ECCO2 is computed as a residual from the mass conservation condition in the horizontal plane. ECCO2, as a depth-coordinate model, may have a preferential advection along z-constant surfaces. Hence, in regions where the isopycnals are notably tilted, these models may lead to an artificial diapycnal flux [*Griffies et al*., 2000]. Nevertheless, as shown by Figure 5 in section 4, this description appears to be accurate enough to reproduce the water mass composition of the naOMZ thermocline.

On the other hand, the eddy-permitting, but not fully resolving, ECCO2 velocity field may underestimate the strength of the tropical system of jets and the horizontal turbulent diffusion. *Duteil et al*. [2014] have shown that the model horizontal resolution, i.e., the model ability to resolve mesoscale structures, plays a major role in reproducing the thermocline oxygen content of the tropical Atlantic. Although we focus on the water mass distribution rather than oxygen content, in order to compensate for this underestimation of small-scale dispersion, subgrid diffusion will be artificially added in the computation of the Lagrangian trajectories as proposed by *Döös et al*. [2011] and briefly summarized below.

2.4. The Lagrangian Experiment

Lagrangian trajectories are computed using the Connectivity Modeling System version 1.1 (CMS) [*Paris et al*., 2013] that tracks virtual particles within a numerical circulation model. An advantage of the CMS package is that it allows adding artificial eddy diffusivity to simulate dynamics with a smaller spatial scale than the model grid resolution. This artificial turbulence is here parameterized by including a stochastic impulse (I) each time step particles are advected. As in *Döös et al*. [2011], this impulse consists of an extra horizontal velocity parameterized according to $I = r\sqrt{2\ K/dt}$, where K is the horizontal eddy diffusivity coefficient, dt is the time step, and r is a random number between -1 and 1 from a Gaussian distribution. In our case, with a 1/4° horizontal resolution model, we tested $K = 0$, 50, 100, and 1000 $m^2\ s^{-1}$, and the best fit to

observations (section 4.1) corresponded to using $K=100$ m^2 s^{-1} together with the original 3-D velocity field. This value is in reasonable agreement with *Döös et al*. [2011] who obtained $K=300$ m^2 s^{-1} as the best fit between the dispersion of real ocean surface drifters and virtual particles within a 1/4° resolution model. The focus on subsurface levels in our study likely explains the smaller values we use for *K*.

In order to discern the role that diapycnal fluxes and the horizontal subgrid-scale diffusion play in the water mass renewal of the naOMZ, we will use four different Lagrangian simulations of increased complexity, corresponding to the 2-D and 3-D velocity fields with and without a subgrid-scale diffusion of $K=100$ m^2 s^{-1} (section 4). Specifically, we will compare the outcomes from the following four simulations: 2-D isopycnal velocity field without subgrid-scale diffusion (ISO-K0); 2-D isopycnal velocity field adding subgrid-scale diffusion (ISO-K100); original ECCO2 3-D velocity field with no added diffusion (3D-K0); and the 3-D velocity field with added subgrid-scale diffusion (3D-K100). In particular, the contribution of the diapycnal fluxes to the water supply will be assessed by comparing the ISO-K100 and 3D-K100 simulations.

As we are interested in the source of the naOMZ waters, we release particles within the naOMZ and advect them backward in time for up to 100 years. This means that we are computing all trajectories that end up in the naOMZ in a realistic forward time simulation. In order to attain a time series 100 years long, the available 20 year numerical simulation is therefore looped in the same way as in *Van Sebille et al*. [2012, 2013]. The release region for the virtual particles, hereafter defined as the naOMZ box, is located between 9°N and 17°N and east of 22°W (Figure 1). This box roughly comprises the climatological vertically averaged contour of 60 μmol kg^{-1} for oxygen content within the 200–500 m depth layer while it also includes the region where most of the lowest oxygen values have been recently located [*Fischer et al*., 2013] at the core of the naOMZ. In each experiment, a total of 170,000 virtual particles are randomly seeded every 15 days during the first 5 years of the simulation. For simplicity, although the Lagrangian simulation is computed backward in time from the naOMZ box, in the manuscript we will describe the particle trajectories in a realistic forward time, always ending in the naOMZ.

The vertical extension of this study covers the CW stratum with the aim of discerning the distinct circulation patterns at depth that lead to the thermohaline transition observed at the σ26.8 density level. Following previous studies in the tropical Atlantic [*Elmoussaoui et al*., 2005; *Rhein et al*., 2005; *Kirchner et al*., 2009; *Peña-Izquierdo et al*., 2012], we will refer to waters with σ_θ between 26.3 and 26.8 kg m^{-3} as the upper CW (uCW) and to waters with σ_θ between 26.8 and 27.15 kg m^{-3} as the lower CW (lCW).

3. Water Mass of the naOMZ

Hydrographic observations in the northeastern tropical Atlantic Ocean show an abrupt thermohaline transition usually centered at σ26.8 [*Voituriez and Chuchla*, 1978]. For any *T/S* diagram in this region, the transition can be easily detected within the CW stratum as a marked salinity depth inversion, sometimes also present in temperature, indicative of a change in the water mass composition. A relatively fresh and cold water mass indicates the presence of SACW in the uCW while the salty and warm water suggests a greater influence of NACW in the lCW. Figure 3 shows this transition as characteristic for the whole northeastern tropical Atlantic, being clearly present as far west as 40°W and as far south as 7°N. In general, the salinity inversion becomes stronger and shallower moving northeastward in the tropical North Atlantic.

This transition is also found in the model climatological mean, with a similar geographic pattern and at the same levels as in the observations (Figure 3, top panels). The main difference is observed near Africa at 20°N, where observations show a region with *T/S* transition profiles at density levels shallower than observed in the model. This difference is likely due to temporary NACW and SACW interleaving in the frontal zone related with eddies or filaments [*Tomczak*, 1981], which are not properly represented by the model climatology that only includes permanent features. Therefore, this ubiquitous hydrographic footprint suggests a permanent and distinct circulation pattern between the uCW and the lCW. Moreover, the vertical distribution of fresher and colder SACW above saltier and warmer NACW avoids the development of salt fingering thus favoring the permanence of this feature in time.

A simple explanation for the formation of the thermohaline transition arises from the spatial distribution of the *T/S* diagrams (Figure 3). Zone A corresponds to the NEUC and nNECC region. The *T/S* diagrams in the naOMZ (zones B and C) indicate the presence within the uCW of pure southern waters advected by these

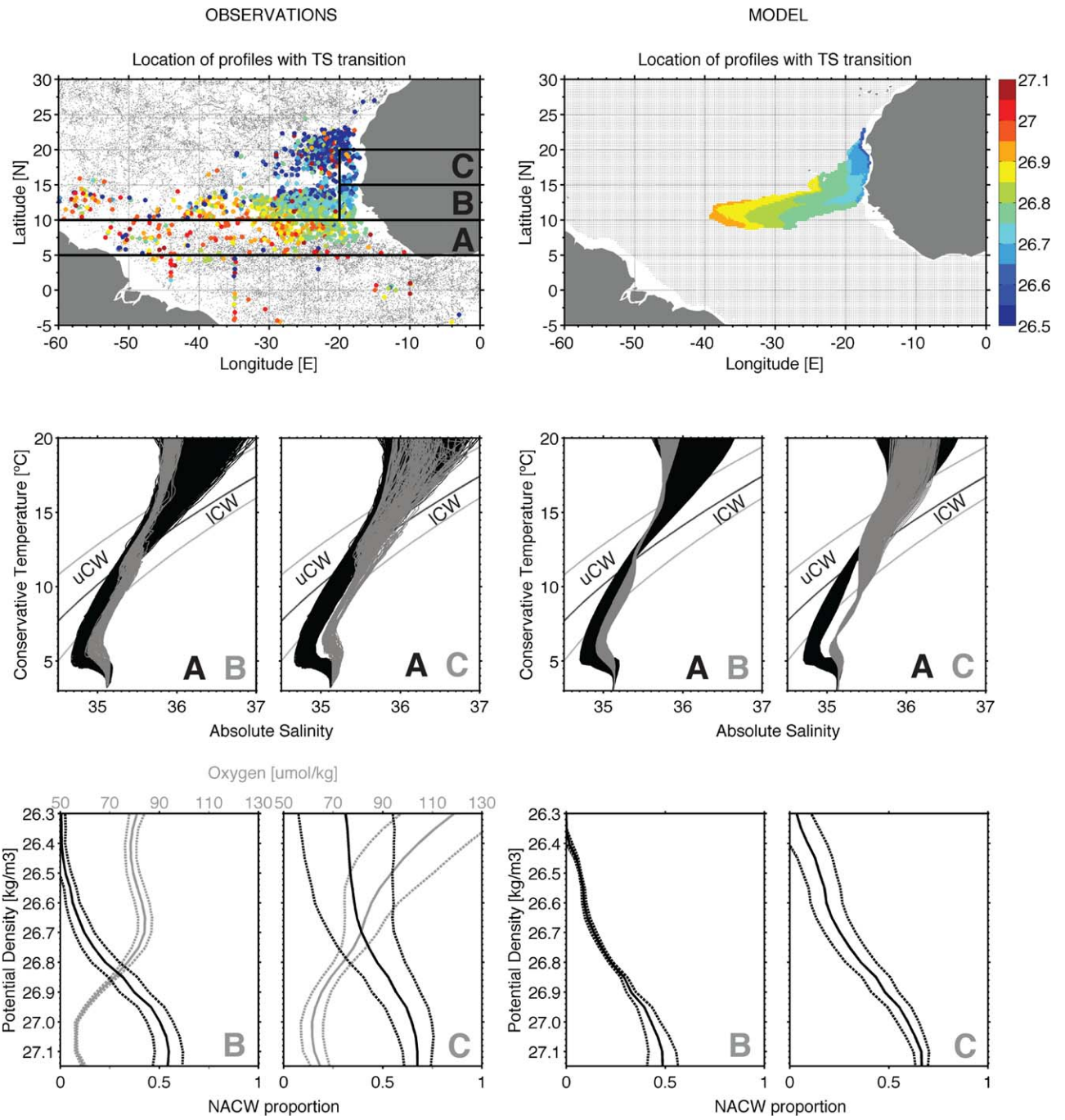

Figure 3. (top) The colored dots show the location of the *T/S* profiles with a marked thermohaline transition, defined as a change in the slope of the *T/S* profiles greater than 0.1°C per salinity unit with respect to the NACW and SACW predefined slopes. The color code indicates the density level where the transition is found. (middle) *T/S* diagrams of those profiles located in the A, B, and C regions shown in the top-left panel, plotted according to the black-gray code shown inside each box; regions B and C include 135 and 109 profiles, respectively. (bottom) Mean profiles of NACW proportion and oxygen content for regions B and C; the dashed lines denote one standard deviation. The left plots are for the observational data set, while the right plots are for the ECCO2 model output. Note that the ECCO2 model does not include the oxygen field.

jets, thus revealing a direct connection with zone A. However, the lack of these southern waters in the lCW of the naOMZ suggests that this connection disappears below σ26.8, particularly in the northern area (zone C).

The water mass analysis helps us understand the exact contribution of southern and northern water masses in the renewal of the tropical North Atlantic upper thermocline (Figure 4). The distributions of NACW and SACW exhibit opposite patterns above and below σ26.8. In the uCW, the SACW stretches north along the

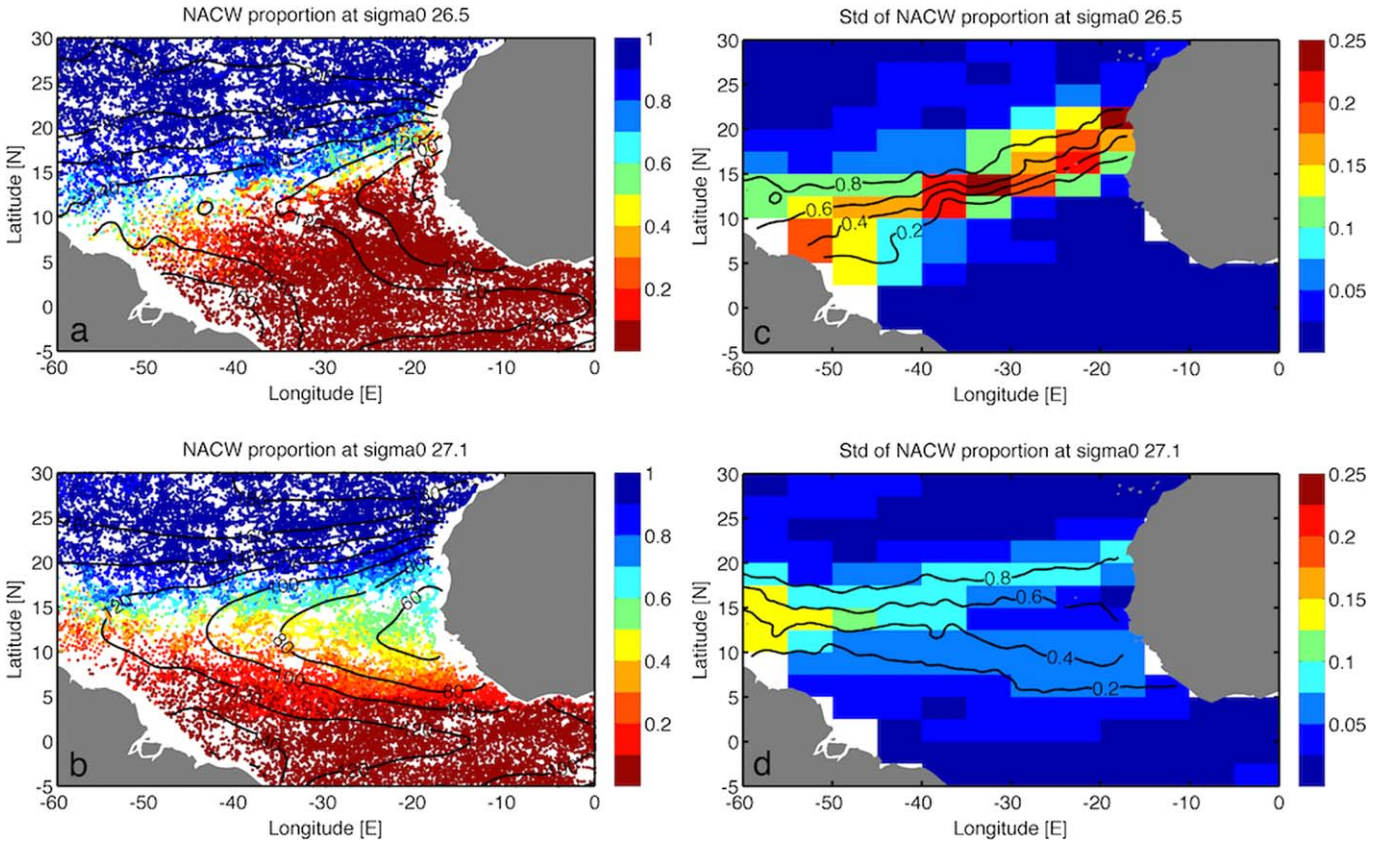

Figure 4. Distribution of CWs in the tropical Atlantic Ocean. (left) Proportion of NACW (color-coded) as deduced from the water mass analysis at (top) σ26.5 and (bottom) σ27.1, where the oxygen content in the uCW and lCW layers is minimum. Black contours show the climatological oxygen field at the respective density levels. (right) Standard deviation of the NACW proportion within bins of 2.5° latitude × 5° longitude (color-coded); all bins include more than 50 observations. Black contours show the smoothed distribution of NACW after a gridding scheme algorithm. The SACW proportion always equals the complementary part of the NACW contribution, i.e., SACW + NACW = 1.

eastern margin while the NACW penetrates into the tropical Atlantic from the western margin. This pattern agrees with the circulation scheme proposed by *Schott et al*. [2008] for the subtropical cell, with an intense northward flow along the eastern margin, especially in autumn [*Elmoussaoui et al*., 2005]. In contrast, in the lCW, the SACW is advected along the American continent toward the Caribbean Sea while the NACW spans southward along the African coast. A similar pattern was suggested by *Poole and Tomczak* [1999] from data before the Argo era, with much lower horizontal resolution. In summary, the naOMZ is dominated by SACW in the uCW while an equally split mixture of NACW and SACW is found in the lCW.

The presence of a large fraction of NACW in the lCW is very relevant for the oxygen supply to the naOMZ because the NACW is more recently ventilated than the SACW, thus having higher oxygen content. Nevertheless, the mean patterns for regions B and C (Figure 4) show that the oxygen concentration decreases just below σ26.8, where the NACW proportion notably increases; in particular, the absolute oxygen minimum is found at σ27.1, exactly where the NACW fraction within the naOMZ is largest. Further, for the lCW, the proportion of NACW is quite homogeneous within the naOMZ, as shown by the local minimum in the standard deviation of this fraction (Figure 4d). The presence in this region of a well-mixed water mass, with a notable contribution of NACW but minimal oxygen content, can be explained by a marked reduction in the water renewal rate within this layer. These results agree with the existence of a regional water mass variety for the naOMZ (the Cape Verde SACW, i.e., SACWcv), as proposed by *Peña-Izquierdo et al*. [2012]. Such regional water mass would explain the presence of two bands of relatively high standard deviations in the eastern Atlantic, south of 10°N and north of 15°N, representative of two different mixing regions: SACW with SACWcv to the south, and SACWcv with NACW to the north (Figure 4d). Therefore, for the lCW, both SACW and NACW would reach the naOMZ while slowly mixing with SACWcv, therefore reducing the oxygen content.

These observations lead to two main questions: What are the water mass pathways that lead to such a vertical water mass distribution? And what role does NACW play in the ventilation of the naOMZ? In the following two sections we will answer these questions with the help of the backward Lagrangian experiments, computing the pathways followed by the water masses that end in the naOMZ at different density levels.

4. Lagrangian Simulations

The contributions of the different water masses that make up certain regions of the ocean can also be inferred from the trajectories of the water parcels, or Lagrangian particles, that end up in that region. Specifically, the analysis of the origin of all particles ending in the naOMZ should be comparable with the water mass analysis carried out in section 3. Both analyses should independently lead to similar water mass contributions to the naOMZ. A good agreement among them should be considered as a consistent validation of the ocean model velocity fields and the inferred Lagrangian trajectories.

4.1. Lagrangian Stream Function

One way to reveal the average pathways of a set of trajectories is to compute a Lagrangian stream function (LSF). Analogous to the standard (Eulerian) stream function, which accounts for the flux between neighboring points at any given time, the LSF accounts for the net number of particles (or trajectories) that flow between two grid points throughout the entire simulation. However, it is important to note that the LSF does not show the average circulation within a region, as the Eulerian stream function does. Instead, the LSF only shows a subset of the circulation, in our case, the pathways to the naOMZ.

To compute a stream function, the flow should always be nondivergent. In the case of a LSF, this means that trajectories should start and end out of the domain. The summation of the latitudinally flowing particles is carried out along parallels, moving east from the western boundary and considering as positive (negative) counts those particles that move north (south), i.e., particles always flow with larger LSF values to the right. We have also taken the zero LSF reference value at the south-western grid point of the domain. These definitions imply that the sign of the LSF is related to the origin of the trajectories; positive (negative) values are related with southern (northern) origin particles. Finally, the LSF values are normalized by the total number of particles, so they represent the proportion of particles that follow a specific pathway. For further details about the LSF computation, the reader is referred to *Blanke et al*. [1999] or *Döös et al*. [2008].

In section 3, we have shown that the thermohaline transition observed at σ26.8 is a permanent feature of the northeastern tropical Atlantic. Such a marked and persistent hydrographic footprint requires a continuous generating mechanism. We suggest that the uCW and lCW should be governed by different dynamics, leading to a continuous supply of distinct water masses in each layer. However, diffusive processes, especially diapycnal fluxes, should counteract this differentiation. To distinguish between developing and erasing processes, we use the following three Lagrangian simulations: isopycnal velocity field and no added subgrid-scale diffusion (ISO-K0), 3-D velocities but no added subgrid-scale diffusion (3D-K0), and 3-D velocities with added horizontal subgrid-diffusion (3D-K100) (section 2.4).

Figure 5 compares, for all three simulations, the mean vertical profile of the observed proportion of NACW within the naOMZ (black line) with the proportion of particles having a northern origin (colored lines). Note that in order to show the Lagrangian pathways within the tropical Atlantic, the LSF is computed between 5°S and 30°N. This implies that particles of southern and northern origin, respectively, come from south of 5°S and north of 30°N. This criterion is potentially too restrictive, as SACW contributes over 80% south of 6°N, and NACW contributes more than 80% north of 20°N (Figure 4). Therefore, we could alternatively assign a SACW fingerprint to those particles arriving to the naOMZ from south of 6°N, and a NACW signature to those particles arriving from north of 20°N. Hereafter, we will distinguish between particles arriving from south/north of 6°N/20°N and the more restrictive definition of particles of southern/northern (5°S/30°N) origin. Notice that, with the less restrictive definition (6°N/20°N), a trajectory starting south of 5°S but flowing between 20°N and 30°N before entering into the naOMZ will be considered as a 20°N particle despite its southern origin. For comparison, Figure 5 shows the profiles following both criteria in each simulation. The two profiles agree in general although, as expected, the 6°N/20°N is closer to the observations for all simulations.

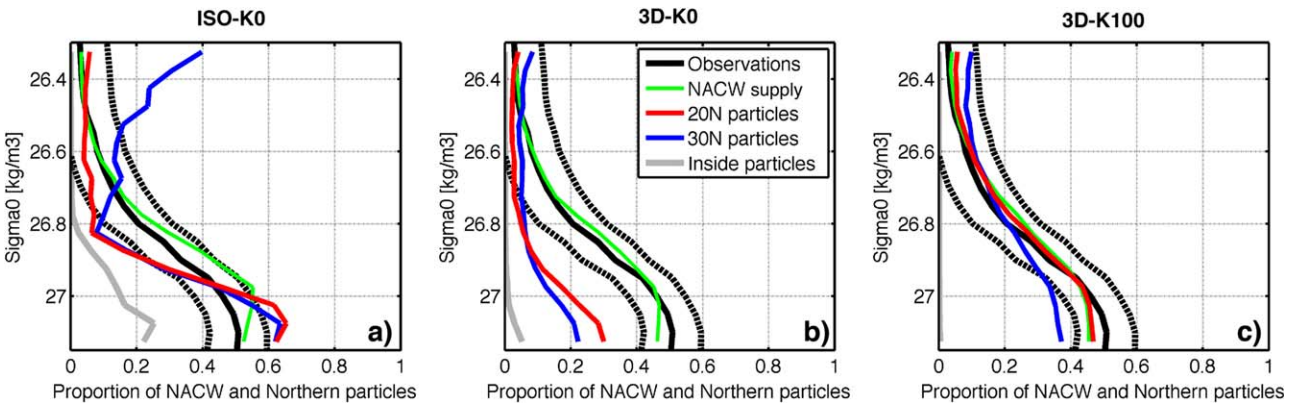

Figure 5. Comparison between the mean observed vertical profile of NACW within the naOMZ box (black line, with the dashed line showing one standard deviation from the mean), and the fraction of particles of northern origin entering the naOMZ (the red/blue lines correspond to particles arriving from north of 20°N/30°N). Additionally, the green line is calculated as the contribution of NACW particles that cross into the naOMZ box, and the gray line denotes the fraction of particles that do not leave the domain during the whole 100 year simulation.

4.2. Water Mass Pathways: ISO-K0

The contribution of northern particles increases markedly with depth near σ26.8 for all simulations, in agreement with observations. However, the transition in the vertical profile is especially abrupt in the isopycnal simulation (ISO-K0, Figure 5a), with a roughly constant 10% contribution of 20°N particles above σ26.8 but increasing largely just below, reaching 63% at σ27.1. This unrealistic abrupt transition between the uCW and lCW is likely due to the neglect of diapycnal fluxes. Nevertheless, this also points to the distinct dynamics that rule the isopycnal circulation in each layer.

The LSF shows very different patterns between the uCW and lCW for the ISO-K0 case (Figures 6a and 6b). For the uCW, the major (above 80%) contribution of southern origin particles (red shading) is displayed via a continuous and successive northward branching from the tropical system of jets toward the naOMZ, throughout the whole zonal basin extension. Most of these particles cross the equator along the American

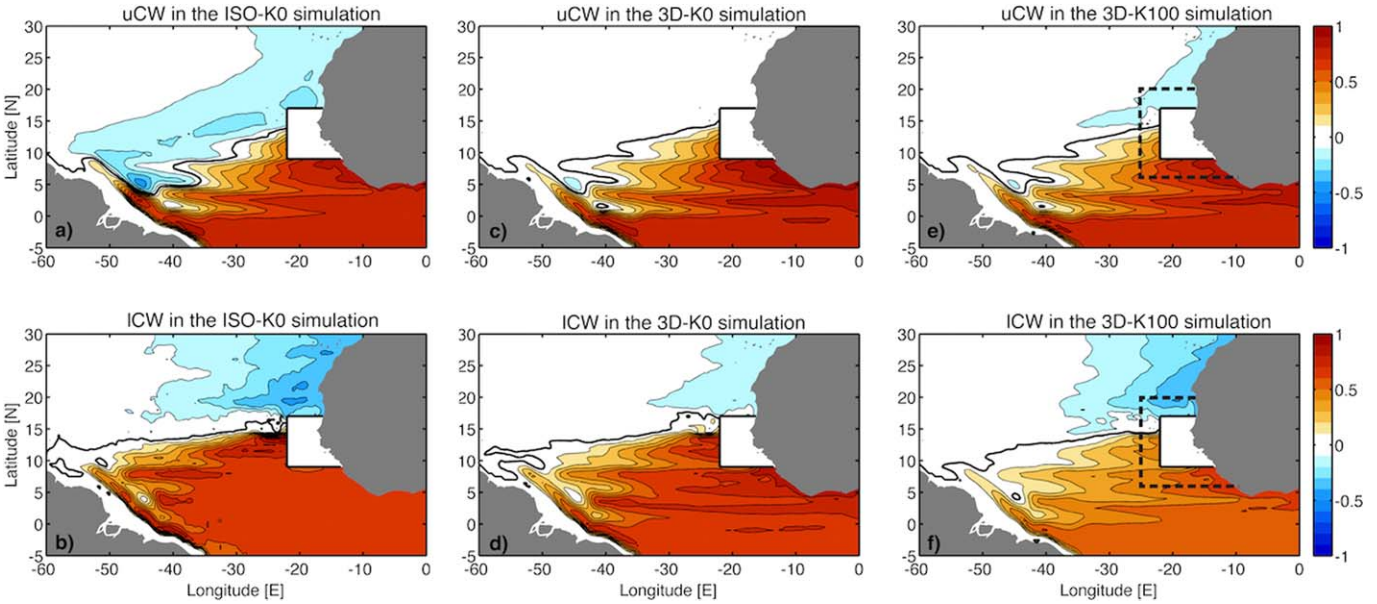

Figure 6. Lagrangian pathways to the naOMZ (black-edged box) for the three experiments within (top) the uCW and (bottom) the lCW. Simulations are from (left) the ISO-K0, (middle) the 3D-K0, and (right) the 3D-K100 runs. The LSF is normalized by the total number of particles per layer, i.e., increments between contours refer to the proportion of particles that flow in between, with LSF values increasing to the right of the flow. The zero reference LSF is selected in the south-western corner of the domain, so positive (negative) values of the LSF are related to southern (northern) origin pathways. The control section used in Figure 8 is displayed as a black-dashed line.

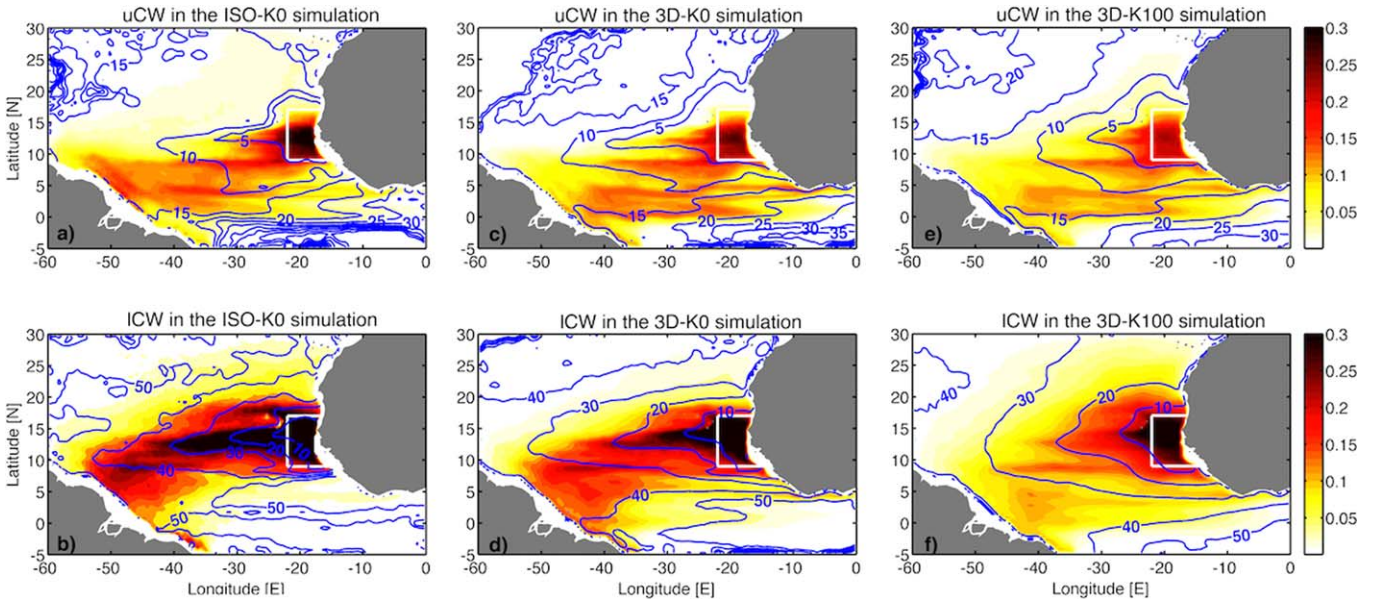

Figure 7. Fraction of the total number of particles (in color) that are found within each 0.5° × 0.5° horizontal bin, at any time during the whole duration of each simulation, for (top) the uCW and (bottom) the lCW strata. Simulations are from (left) the ISO-K0, (middle) the 3D-K0, and (right) the 3D-K100 runs. The advection times to the naOMZ (white-edged box) are displayed with blue contours. For each bin, the advection time is estimated as the median value of the traveling time distribution that particles at the bin location take to reach their seeding location.

continent via the NBC and then retroflect east to feed the EUC at 0°N and the NEUC at 4°N. East of 40°W, northward branching of these jets joins the nNECC flow at about 8°N. Similarly, the nNECC successively branches as it moves north, before entering the naOMZ mostly within a broad latitudinal band between 10°N and the Cape Verde Islands. Northern origin particles (blue contours) within this layer enter the tropics mainly through the western margin, retroflecting east from the southwestward subtropical gyre flow, in agreement with observational studies [*Kirchner et al*., 2009]. However, the contribution of northern origin particles is overestimated (Figure 5a) likely as a result of the inability of the isopycnal simulation to properly reproduce the outcropping of the lighter isopycnals north of 20°N.

For the lCW (Figure 6b), the LSF computed from the ISO-K0 simulation displays three main differences in comparison with the uCW. The first difference, as previously shown in Figure 5a, is the notable contribution of northern origin particles. They retroflect eastward from the main southwestward flow off the eastern boundary, just north of the Cape Verde Islands, and eventually reach the naOMZ directly from this zonal current or after recirculating south along the continental slope. The second difference is the main pathway followed by southern origin particles. They enter into the tropical North Atlantic also via the NBC and retroflect to directly feed the nNECC at about 8°N. Virtually all southern origin particles leave the nNECC before 30°W, branching north into a progressively narrowing band of eastward flow. This occurs just south of 15°N, in what appears to be the main conduit of southern origin particles to the naOMZ in this lower layer. The simulation reveals that, within the lCW and in contrast with the uCW, there is essentially no pathway from the tropics to the naOMZ east of 30°W and south of 10°N.

Finally, the third difference between the uCW and lCW pathways relates to their time scales. Figures 7a and 7b (blue lines) display the average time (in years) required by particles to reach the naOMZ box from any point of the domain. For example, we can compare the regions where southern and northern origin particles enter into the tropical North Atlantic, via the NBC across the equator and via the southwestward flow of the NEC between 20°N and 25°N, respectively. No matter the origin, the times are similar within a layer: between 10 and 15 years for the uCW and between 40 and 50 years for the lCW. The isopycnal simulation suggests that the time scale is 3–4 times longer in the lCW than in the uCW. The advection times show, for the lCW, a notable disconnection between the naOMZ and the region lying just south, with transit times over 50 years for a distance shorter than 3° of latitude (Figure 7b).

4.3. Water Mass Pathways: 3D-K0

When Lagrangian particles are allowed to change their density level along their trajectory (3D-K0), the abrupt vertical transition between the uCW and the lCW is greatly smoothed (Figure 5b). The exchange of particles between different density levels leads to a homogenization in the water mass supply to the naOMZ. Some of the particles originally at less dense levels, thus of a predominant southern origin, will finally end within the naOMZ at more dense levels, explaining the reduction of northern particles in the lCW. This feature is also noticeable in the LSF of the lCW layer (Figure 6d): the pathways followed by the particles ending in the lCW of the naOMZ now resemble those followed by the uCW particles. In this simulation, roughly 30% of all lCW particles reach the naOMZ directly from the nNECC (south of 10°N) or from even further south. This circulation is very different from the isopycnal simulation (Figure 6b) where this pathway is totally absent. Additionally, the advection times within the lCW are reduced by about 25% (Figure 7d). In contrast, the contribution to the uCW of northern particles is still minimal, i.e., no transfer from deeper levels is observed. Consistently, the general scheme of the LSF and the advection times for uCW are only slightly modified with respect to the ISO-K0 simulation. This asymmetry in the vertical transfer of particles between the two layers will be detailed in section 4.5.

On the other hand, the diapycnal fluxes in the 3D-K0 simulation underestimate the contribution of the northern particles, especially in the lCW (Figure 5b). This suggests there may be other processes playing an important role in the water mass renewal of the naOMZ. The next section addresses this question.

4.4. Water Mass Pathways: 3D-K100

Mesoscale dynamics may play a major role in the renewal of the OMZ thermocline [*Duteil et al*., 2014; *Hahn et al*., 2014]. Since the eddy-permitting ECCO2 model does not fully resolve those processes responsible for the generation of mesoscale eddies, the ventilation of the naOMZ may be underestimated (Figure 5b). For this reason, in our Lagrangian approach, the effect of the unresolved eddies is simulated by adding horizontal subgrid-scale diffusion to the model trajectories (3D-K100 simulation, see section 2.4).

The added horizontal diffusion enhances the proportion of northern particles, so that it becomes remarkably similar to the observational profile (Figure 5c). This added diffusion has two main effects. First, it leads to a substantial increase in the water transfer from the northern subtropical gyre across the frontal zone, particularly in the lCW where the mean flow is sluggish. The added diffusion increases the number of northern origin particles leaving the subtropical gyre and entering the naOMZ via the eastward flow just south of 20°N (Figure 6f), as also seen in the ISO-K0 simulation (Figure 6b). The second effect is to strengthen the northward transfer from the NEUC and nNECC. As a consequence, the advection times (Figures 7e and 7f) from the subtropical gyre and the north equatorial jets into the naOMZ are reduced (20–30%) compared with the two previous simulations. This is especially relevant for the supply of oxygen, as it implies an enhanced connection from these more oxygenated regions (Figure 1) and thus a more efficient ventilation of the naOMZ.

For the 3D-K100 simulation, a more detailed description of the water supply to the naOMZ is presented in Figure 8. It shows the inflow of particles across a control section located 3° outside the naOMZ box, where particles are released, distinguishing the preferential pathways into the naOMZ. Since particles may cross this control section several times, we only show where and when they cross it for the last time before reaching the naOMZ box. The results of the 3D-K100 simulation may also be used to calculate the fraction of NACW that enters the naOMZ box at different levels. This supply is calculated as the observational proportion of NACW at the location where each particle enters the box, and then adding the contributions for all arriving particles. The profile of this NACW supply (green line in Figure 5) fits the observations remarkably well in all simulations, although becomes progressively better as we introduce diapycnal fluxes and added diffusion. The goodness of this agreement, which depends on both the particle pathways and the NACW content at the location where the particles enter the box, grants further confidence to the model velocity field, i.e., if the entry pathways were incorrect then the NACW supply would differ from the proportion of NACW observed within the naOMZ box.

Several inflows are clearly distinguished in Figure 8 and their contribution to the total supply is summarized in Table 1. Within the uCW, the shallow northward NEUC branch and the direct inflow of the nNECC are the major contributors (56%), with only a minor inflow arriving north of the Cape Verde Islands (5%). For the lCW, the water supply is more northerly: the combined contribution of the NEUC and nNECC is halved

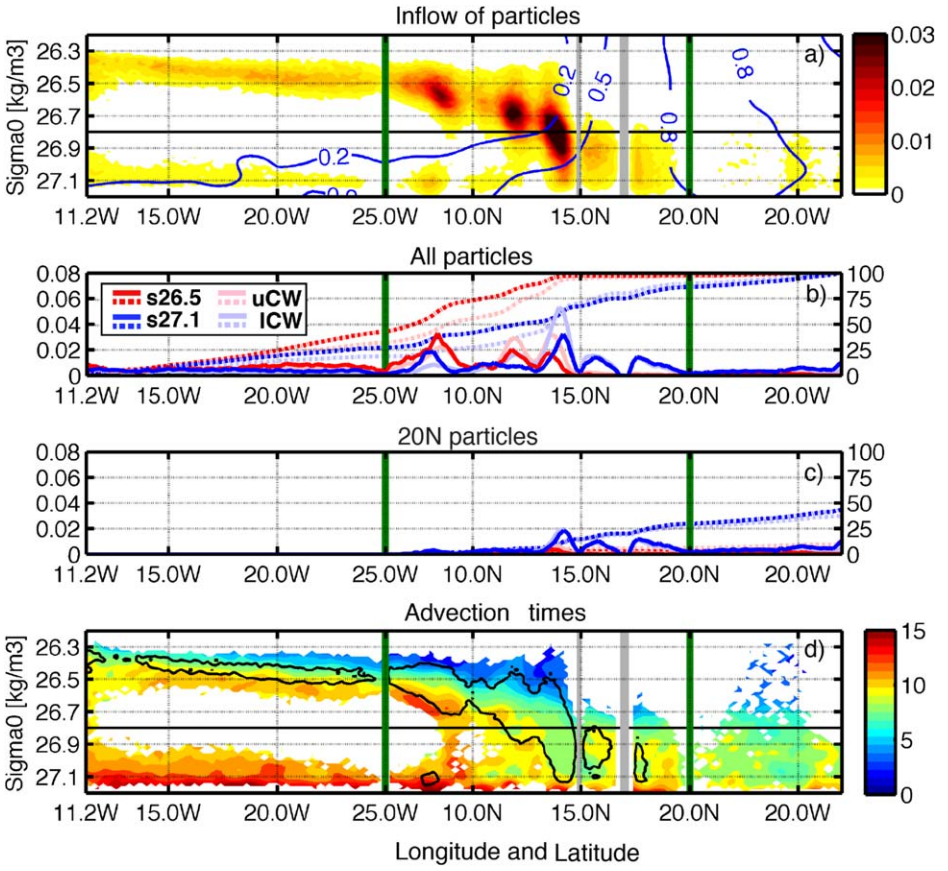

Figure 8. Water supply across the naOMZ control section in the 3D-K100 simulation (Figures 6e and 6f). (a) Fraction of the total number of particles crossing the control section at each density level (colored) together with the proportion of observed NACW (blue contours). (b) The normalized local inflow (solid lines) and along-section cumulative inflow (dashed lines) of particles according to level and layer (see inset legend). (c) As in Figure 8b but for particles originated north of 20°N. (d) Average advection time (in years) between the moment particles cross the naOMZ control section and the moment they reach their seeding location; for comparison, the contour of 0.005 units in the fraction of ingoing particles (displayed in Figure 8a) is shown with a black line.

(28%), a pronounced maximum inflow is found centered at 14°N (29%), and the inflow north of the Cape Verde Islands is doubled (30%). At the core of the naOMZ (σ27.1), a major contributor (27%) is the northward flow arriving from south of 6°N; since the ISO-K0 simulation shows a negligible inflow south of 6°N, the conclusion is that this inflow is primarily driven by diapycnal fluxes and enhanced eddy diffusion. Nevertheless, the zonal flow north of the Cape Verde Islands contributes nearly one third of the total water supply to the naOMZ, in remarkable contrast with the importance traditionally assigned to the southern pathways (NICC and nNECC). Moreover, it is noteworthy that the contribution of 20°N particles reaches up to 45% at σ27.1 (Figure 5c); this is a substantial increase compared with the other simulations, yet less than the 50% observed fraction of NACW (Figure 3), thus the supply from the northern subtropical gyre at this level is still slightly underestimated in this simulation. Additionally, the mean advection times for arrival from the control section to the naOMZ box (Figure 8d) are much shorter for the northern pathways than for the southern ones.

Table 1. Contribution (%) of the Different Streams Through the Control Section, Supplying Water Mass to the naOMZ for Both the Upper Central Water (uCW) and Lower Central Water (lCW) Strata[a] (See Section 4.4)

		NEUC/NICC	nNECC	12°N	14°N	16°N	18°N	20°N
Total	uCW	**32** (**43**)	24 (31)	22 (16)	17 (18)	01 (00)	01 (00)	03 (02)
	lCW	18 (**27**)	09 (14)	14 (10)	**29** (16)	10 (08)	09 (11)	11 (14)
Northern	uCW	00 (00)	00 (00)	01 (01)	**03** (**02**)	00 (00)	00 (00)	**03** (**02**)
	lCW	00 (00)	01 (02)	03 (04)	10 (09)	05 (05)	08 (09)	**11** (**14**)

[a]The values in parenthesis correspond to the σ26.5 and σ27.1 levels and the bold numbers emphasize those flows with the highest contributions; northern refers to the proportion of the total flow formed by northern origin (30°N) particles (Figure 8c).

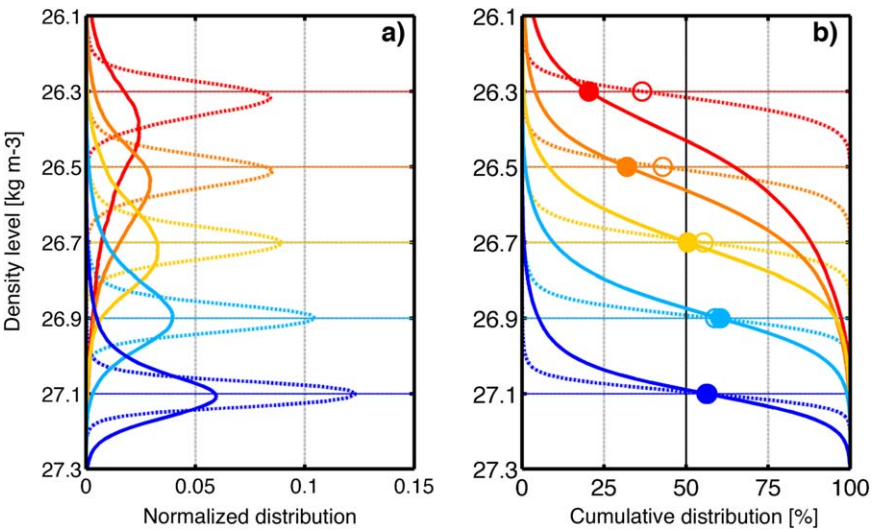

Figure 9. (a) Potential density distribution for five sets of particles (each set uses a different color) corresponding to 1 and 10 years (dashed and solid lines, respectively) before they reached the naOMZ. Particles for each set end their trajectory in the selected density level (σ26.3, σ26.5, σ26.7, σ26.9, and σ27.1). (b) Corresponding cumulative distributions, with circles highlighting the proportion of particles with densities smaller than the final density level. Note that more (less) than 50% of the particles ending at a specific density level above (below) σ26.7 originally had larger (smaller) densities.

4.5. Diapycnal Component

The changes in the pathways from the ISO-K0 to the 3D-K0 simulations indicate a remarkable role of the mesoscale and regional-scale diapycnal advection in the renewal and vertical redistribution of the naOMZ water mass, especially within the lCW. To understand how this occurs, we look at the evolution of the density distribution of particles ending at several density levels within the naOMZ (Figure 9). The density distributions are Gaussian-like, approximately centered around the ending density level as expected for isotropic vertical mixing arising from small-scale processes (double diffusion and shear-induced). However, for some destination levels, there are significant net upward or downward deformations (Figure 9a). Particles ending in the upper levels of the naOMZ, above σ26.7, come mainly from higher densities thus pointing to upward diapycnal velocities (Figure 9b). Conversely, below σ26.7, particles mostly have a lighter density origin, i.e., downward diapycnal velocities. These contrasting vertical motions within the uCW and lCW contribute to the distinct horizontal patterns for these two layers, as shown in the previous sections.

Nonetheless, these vertical motions should be taken with caution since, as noted in section 2.3, z-coordinate models as ECCO2 may induce spurious diapycnal diffusion especially in those levels where the isopycnals are more vertically slanted, such as in the upper levels. In order to verify whether the diapycnal processes leading to the distributions are within realistic values, we compare the vertical dispersion of our numerical particles (Figure 9) with the GUTRE tracer experiment in the naOMZ [*Banyte et al.*, 2012]. On one hand, the shape of the vertical distribution after the first year of the backward simulation (dotted lines in Figure 9) is quite symmetric and accurately resembles quantitatively the Gaussian distributions observed in *Banyte et al.* [2012] for the first 2 years after the tracer release. On the other hand, we estimate the mean diapycnal velocity as the temporal rate of change in the average density of a subset of particles ending at a certain density level (Figure 9b); we assign this average density to the median of the density distribution at a given time. The mean diapycnal velocities calculated in this way range between $+4.1 \times 10^{-10}$ kg m^{-3} s^{-1} in the upper levels and -1.8×10^{-10} kg m^{-3} s^{-1} in the lower levels. The average diapycnal velocity obtained by *Banyte et al.* [2012] at σ26.9 was $+1.5 \pm 2.7 \times 10^{-10}$ kg m^{-3} s^{-1}, slightly smaller but of the same order of magnitude as our estimates. These results grant us confidence on the realism of the numerical simulation, indicating that the diapycnal fluxes deduced from the Lagrangian experiment are not grossly biased by spurious diapycnal diffusion. The estimated net diapycnal flux can thus be attributed to a real regional-scale process that is reasonably well reproduced in the ECCO2 model.

The exchange of particles between distinct density levels (Figure 9) points out that diapycnal fluxes should have an impact on the naOMZ renewal times, as different levels have different advection times (Figure 7).

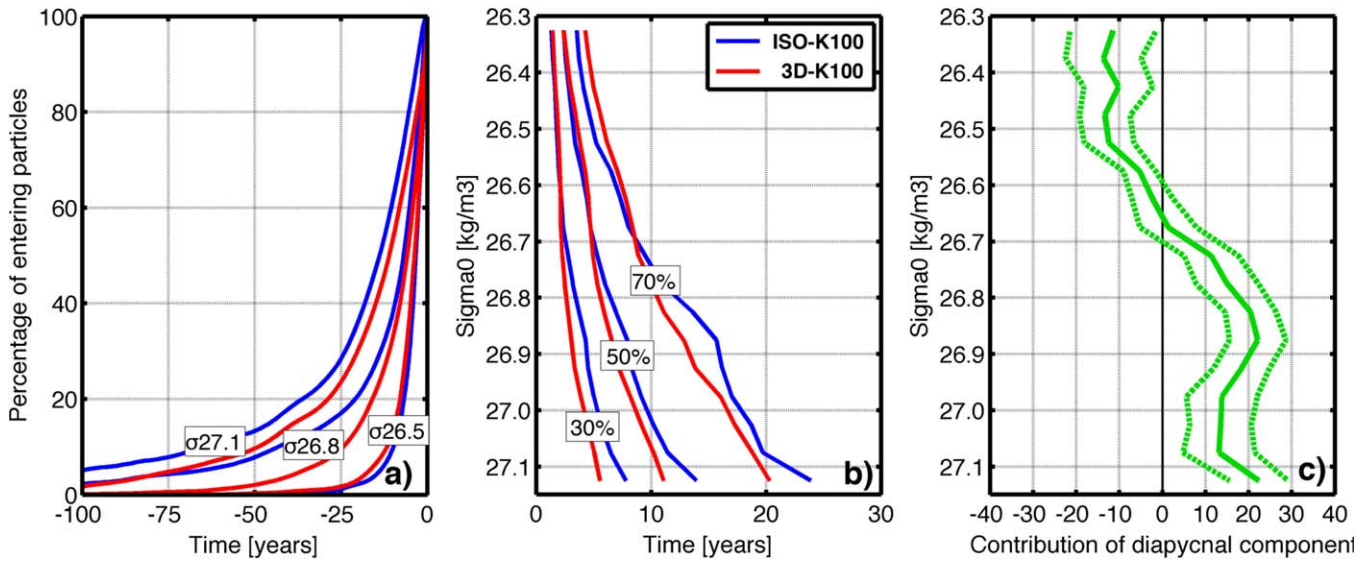

Figure 10. Results from the ISO-K100 and 3D-K100 simulations (blue and red lines, respectively). (a) Temporal increase in the proportion of particles as they fill the naOMZ control region (shown in Figure 6) for three different final density levels; the naOMZ is assumed to be completely renewed when the proportion of particles reaches 100%. (b) Number of years required to fill 30, 50, and 70% of the naOMZ control region, plotted as a function of the final density level. (c) Vertical profile of the contribution of the diapycnal flux to the renewal of the naOMZ (f_{dia}), with positive/negative values representing enhanced/reduced diapycnal water supply; the mean (solid line) and standard deviation (dashed lines) are calculated from the contributions at different times throughout the simulation.

We can quantify the contribution of this diapycnal component in the renewal of the naOMZ water mass by comparing the Lagrangian simulations with and without diapycnal fluxes (3D-K100 and ISO-K100). The only difference between the two outcomes will respond to meso and regional-scale diapycnal fluxes. A first step is computing the function, $n(t)$, that counts the amount of particles within the naOMZ as a function of time, thereby identifying the time scales of water mass renewal (Figure 10a). When this function reaches 100%, the naOMZ is completely renewed, full of particles; this moment corresponds to the beginning of the backward simulation. From this function, inferring the renewal times (the required time to renew a certain percentage of the whole naOMZ water mass) is straightforward (Figure 10b). The inflow of particles toward the naOMZ is given by the change of $n(t)$ in time, $F(t)=dn/dt$. We may then compute the purely isopycnal inflow, $F_{iso}(t)$, obtained from the ISO-K100 simulation and the isopycnal + diapycnal inflow, $F_{3D}(t)$, from the 3D-K100 experiment. The effect of diapycnal fluxes in the water mass renewal of the naOMZ is quantified as $f_{dia}(t)=F_{dia}/F_{3D}=(F_{3D}-F_{iso})/F_{3D}$.

Figure 10c shows the average vertical profile of f_{dia}. Below σ26.7, f_{dia} is positive because a large proportion of particles ending at these levels come originally from lighter and swifter levels (Figure 9b). As a consequence of this prevailing downwelling, the water supply to the naOMZ is enhanced by about 10–20% within the ICW. On the other hand and within most of the uCW, the predominant upwelling leads to a 10% weakening of the water mass renewal.

5. The Upper Thermocline Circulation in the ECCO2 Model

5.1. The Northeastern Tropical Atlantic

We may now connect the features that have emerged from the Lagrangian analysis with the general circulation of the northeastern tropical Atlantic as deduced from the model. We start by investigating the Eulerian layer-averaged velocity fields. In the uCW, the model shows a broad cyclonic pattern dominating the annual mean circulation (Figure 11a). The mean eastward flow south of the Cape Verde Islands carries water from the tropical to the subtropical regions through a marked northward detour between 30°W and the African continent. This flow is especially enhanced along the continental slope by the PUC, associated with the coastal upwelling system [*Barton*, 1989; *Mittelstaedt*, 1991; *Peña-Izquierdo et al*., 2012]. Similar results arise from the numerical simulation of *Elmoussaoui et al*. [2005], with a maximum northward transport

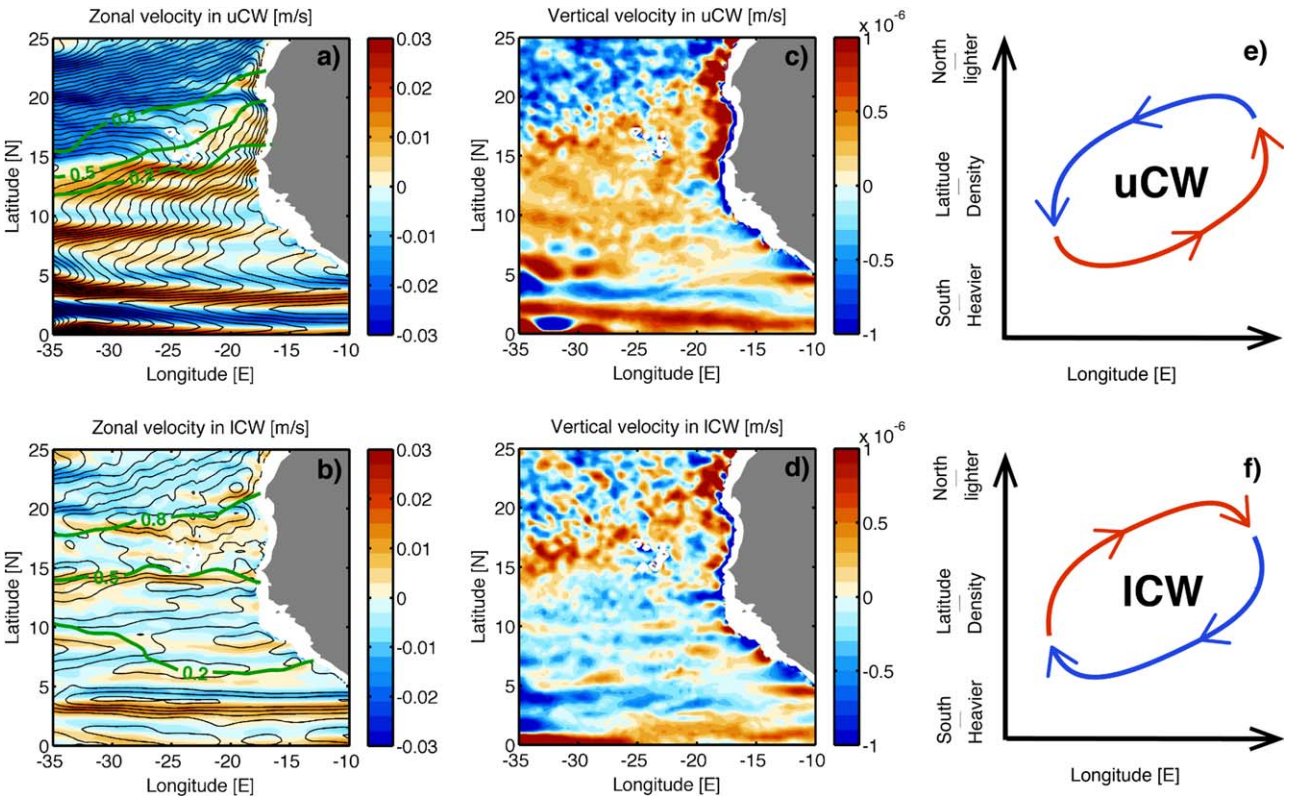

Figure 11. Flow patterns in the northeastern tropical Atlantic Ocean as deduced from the climatological ECCO2 annual-mean flow field. Vertically averaged zonal velocity (in color) for (a) the uCW and (b) the lCW strata; positive values denote eastward flow. Black contours denote the Eulerian stream function with 0.1 Sv increments; green contours represent the averaged NACW proportion within the corresponding layer. (c, d) Analogous plots but for the vertical velocity, with the positive values denoting upward flow. (e, f) Simplified schemes of the 3-D circulation in both layers.

(including now the uCW and the surface layer) of 4 Sv during boreal fall. After joining the westward flow of the subtropical gyre, some of this water recirculates south toward the tropics and then eastward again via the nNECC and NEUC [*Fratantoni et al*., 2000].

The cyclonic tropical path forms part of a complex basin-wide recirculation scheme that also includes upwelling along the eastern tropical edge and subduction along its boundary with the southeastern subtropical gyre, the so-called subtropical cell (STC) [*Zhang et al*., 2003; *Schott et al*., 2004; *Hazeleger and Drijfhout*, 2006]. Further evidence of this pattern can be found in the mean vertical velocity (Figure 11c). As previously revealed from the Lagrangian trajectories, the uCW of the naOMZ is influenced by upwelling, largely enhanced near the continental slope likely due to the coastal upwelling system. North of the Cape Verde Islands, a predominant downward velocity is found related to the subtropical gyre subduction. It is also important to distinguish the Guinea Dome from the STC, the former being a much smaller-scale system acting at shallower levels, located further south and directly driven by the regional cyclonic wind stress [*Siedler et al*., 1992; *Lázaro et al*., 2005].

In the lCW, the mean velocity field is relatively weak, with a circulation pattern less defined than in the uCW (Figure 11b), yet two main structures can be detected. The first one is an anticyclonic gyre located south of the Cape Verde Islands, made up of a well-defined eastward flow at 14°N, all the way from at least 35°W to the African continent, and a southwestward recirculation reaching as far south as 10°N. This pattern therefore weakens the direct penetration of water from the south to the naOMZ. A similar anticyclonic circulation, as deduced from geostrophic calculations, was proposed by *Reid* [1994] for the AAIW layer, located below σ27.15. The southward extension of the contour with 20% content of NACW (Figure 11b) corroborates that this gyre reaches the CW stratum. Furthermore, the existence of a relatively closed anticyclonic circulation also agrees with the observed standard deviation minimum in NACW proportion (Figure 4d),

indicating the presence of a well-mixed water mass, the previously mentioned SACWcv [*Peña-Izquierdo et al*., 2012].

The second lCW structure is the cyclonic recirculation of part of the subtropical waters (with high proportion of NACW) via a predominant eastward flow centered at 18°N. Part of the water recirculates northward but some joins the southern anticyclonic gyre through a southward flow along the slope, south of 18°N. Recent velocity observations during the fall season along the African continental margin [*Peña-Izquierdo et al*., 2012] have shown a similar circulation pattern for the uCW and lCW layers. They suggest a convergent meridional flow at 22°N in the uCW and divergent at 18°N in the lCW. Thus, south of 18°N the continental slope current system is made up by an intense PUC in the uCW and an enhanced southward flow in the lCW, in agreement with the model velocity field. The mean vertical velocity within the lCW (Figure 11d) also displays an opposite pattern as compared with the uCW: predominant downwelling/upwelling taking place south/north of the Cape Verde Islands.

The opposite horizontal and vertical patterns in the uCW and lCW strata resemble the scheme of stacked meridional overturning cells proposed by *Wang* [2005] for both sides of the equator. The upper cell, the so-called tropical cell [*Lu et al*., 1998] occupies the upper 100 m and is made up by the equatorial Ekman-driven upwelling, surface poleward flow until the downwelling band at 3°–4° of latitude, and equatorward flow at the subsurface. The lower cell, named the subthermocline tropical cell [*Wang*, 2005], has a weak circulation between 100 and 300 m, with a pattern opposite to the tropical cell. Analogously, we propose for the northern part of the tropical Atlantic, and for larger spatial and temporal scales, a very simplified arrangement of stacked meridional overturning cells within the uCW and lCW. The upper cell (Figure 11e) would correspond to the subtropical cell while the lower one (Figure 11f) would respond to a lower subtropical cell with reversed flow direction. No direct observations of this two-cell system are available, yet the simplified layered circulation model discussed by *Fratantoni et al*. [2000, Figure 15] also appears to capture the opposing vertical velocity fields that correspond to the opposing cells.

While a detailed understanding of the processes that lead to such a complex 3-D circulation is beyond the scope of this work, we may look for some hints in the structure of the thermocline. The distributions of the depth and thickness of the uCW and lCW (Figure 12) suggest the existence of a baroclinic mode of circulation: those regions with a relatively thick uCW layer have a correspondingly thin lCW layer and vice versa. The similarity between the observed circulation patterns and the bottom depth of each layer suggests that the flow might be approximately represented with a 3.5 layer geostrophic model (three active layers and a quiescent fourth layer [see, e.g., *Xuang*, 2010]. The surface layer would correspond to the layer directly driven by Ekman pumping. The second and third layers would correspond to the uCW and lCW layers and the fourth layer, formed by deeper waters, would be passive. Let us call z_u and z_l the depths where we find the bottom of the uCW and lCW layers. According to this simple geostrophic layered model, the stream function for the third layer (lCW) would match the contours of constant z_l (Figures 11b and 12b), and the streamlines for the second layer (uCW) would follow contours of constant $z_u + z_l$; since the horizontal gradients of z_u are substantially larger than those for z_l, this means that the streamlines in the second layer will approximately follow the contours of constant z_u (Figures 11a and 12a). Therefore, the circulation patterns in the uCW and lCW layers display opposite directions, as expected for a baroclinic mode of oscillation in a layered ocean.

A complementary explanation for these distinct patterns comes from requirements of potential vorticity (PV) conservation by water parcels (Figures 12e and 12f). The predominant stretching of the uCW in the naOMZ region limits the transfer of water from the subtropical gyre. In order to preserve the PV, a southward displacement of a water parcel, thus a stretching, should be balanced by an increase in its planetary vorticity, i.e., a northward displacement. This is the principle for the existence of the shadow zone in the classical theory of the thermocline ventilation [*Luyten et al*., 1983]. However, the opposite situation occurs in the lCW: the thinning of this stratum favors the existence of a southward flow, manifested by the southward deformation of the PV contours and revealing a water transfer from the subtropical gyre within the lCW.

5.2. The Cape Verde Current System

Our analysis on the renewal of the naOMZ relies largely on how realistic the ECCO2 velocity field is. Support comes from the good agreement between the water mass distributions within the naOMZ, deduced either from observations or from the simulated Lagrangian pathways (Figure 5). For further validation, we now

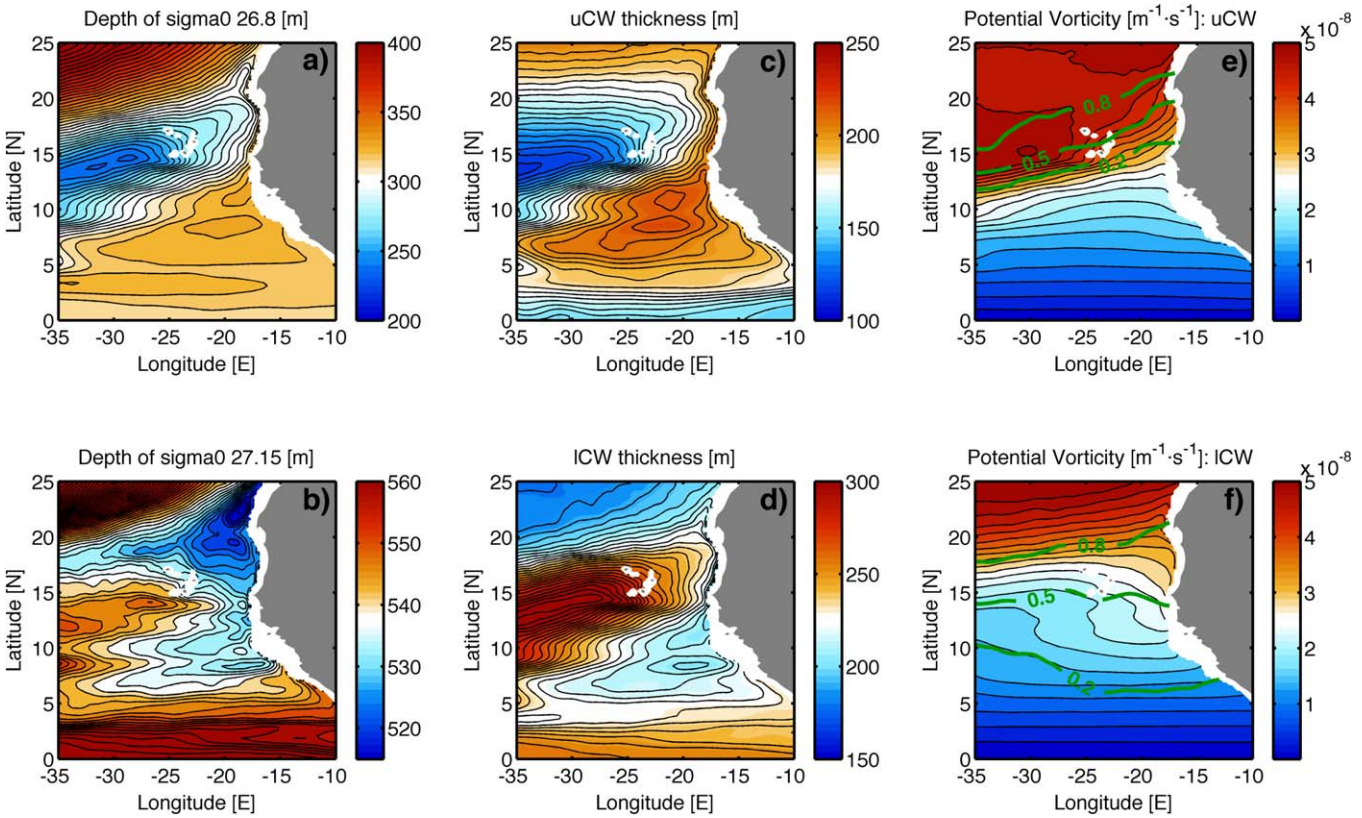

Figure 12. Annual-mean depth of the (a) σ26.8 and (b) σ27.15 density levels, respectively located at the base of the uCW and lCW layers; the contour intervals are 4 m and 2 m for the upper and lower layer, respectively. (c, d) Mean thickness for the uCW and lCW strata, respectively; contour intervals of 5 m. (e, f) Planetary component of the potential vorticity for both the uCW and lCW strata, respectively; green contours represent the average proportion of NACW.

proceed to compare the annually averaged ECCO2 field along a meridional section at 25°W with previous observational studies.

The pathways displayed in Figure 6 are evidence of the characteristic zigzag circulation pattern within the tropical ocean, with a net eastward motion (NEUC at 4°N and nNECC at 8°N–9°N). Our results also reveal the prevalence of other eastward currents reaching as far north as 18°N, playing a remarkable (and not yet properly acknowledged) role in the water supply to the naOMZ (Figure 8 and Table 1). The most notable of these inflows is found at 14°N, clearly traceable in ECCO2 down to 800 m (Figure 13a). These modeled currents agree well with the velocity fields as determined from several observational studies for the CW stratum in this area. Acoustic Doppler Current Profiler (ADCP) observations along 23°W in July 2006 [*Stramma et al*., 2008b] show an intense eastward current at 14°N, reaching 0.2 m s^{-1} in the uCW and 0.1 m s^{-1} in the lCW. In the same study, the time-averaged zonal velocity field deduced from trajectories of autonomous floats drifting at 200 m depth (i.e., in the uCW) shows peak eastward flows of 0.05 m s^{-1} again at 14°N. Furthermore, the average zonal flow computed from several meridional sections, carried out during different seasons between 1999 and 2008 and between 28°W and 23°W [*Brandt et al*., 2010], displays an intense eastward mean flow at 14°N, exceeding 0.1 m s^{-1} in the whole CW stratum. *Brandt et al*. [2010] suggested this current was a recirculation around the Cape Verde Islands but our results show that it flows all the way from the western Atlantic margin to the African continent, although it also includes water recirculating from the south.

A number of observations [*Stramma et al*., 2005, 2008b; *Brandt et al*., 2010; *Hahn et al*., 2014] suggest substantial flow variability between 10°N and 13°N, yet with preferential westward/eastward paths south/north of 12°N, similar to the ECCO2 mean field (Figure 13a). North of the Cape Verde Islands, there are very few velocity observations. A lowered ADCP (LADCP) section along 28°W in summer 2003 displayed a dominant mean eastward flow between 12°N and 18°N only for the 300–600 m layer (i.e., roughly the lCW stratum)

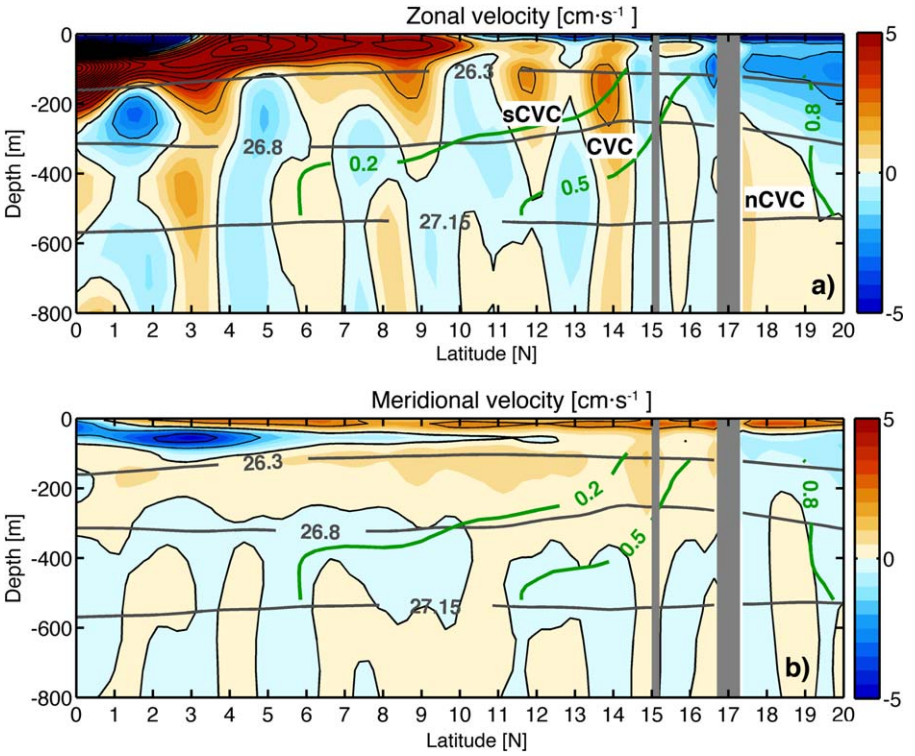

Figure 13. Annual-mean (a) zonal and (b) meridional velocity components along 25°W as deduced from the ECCO2 model. Positive values denote eastward and northward flow; contours of 0.02 m s^{-1} are shown with black lines. Thick gray lines represent the density levels that confine the uCW and lCW layers. The observed NACW proportion is denoted with green contours. The gray vertical shades correspond to two of the Cape Verde Islands.

with velocities at 14°N and 17°N above 0.05 m s^{-1} [*Stramma et al*., 2008b], again in agreement with the ECCO2 results.

The nNECC is also realistically reproduced in the model, located between 8°N and 9°N and covering most of the thermocline. However, further south, important discrepancies with observations appear. The most notable is the absence of the Equatorial Intermediate Current within the lCW. The NEUC is reproduced somewhat further south than observed, connecting at 2°N with the North Intermediate CounterCurrent, a link that does not seem to occur in the real ocean [*Brandt et al*., 2010]. These issues are likely due to the limited horizontal resolution of ECCO2, as high resolution appears necessary to properly model the intermediate-depth equatorial circulation [*Duteil et al*., 2014]. Nevertheless, the Lagrangian pathways (Figure 6) have revealed that the lCW of the naOMZ is only weakly linked to this equatorial region so we expect that the significance of these differences is likely small. This disconnection is evident in the mean meridional velocity field, further supported by the southward extension of NACW along 25°W (Figure 13b).

The existence of prevailing eastward geostrophic undercurrents far from the equator (north of 10°N), as calculated using the Argo program *T/S* profiles, has been recently reported for the North Pacific Ocean by *Qiu et al*. [2013a, 2013b]. These authors found subsurface eastward jets located at 9°N, 13°N, and 18°N in the western Pacific margin. The vertical extension of these jets may reach down to 1000 m, with the upper limit typically varying between σ26.0 and σ27.0 and shoaling eastward. These "NEUC jets," as *Qiu et al*. [2013a, 2013b] dubbed them, seem to be good candidates for the eastward currents observed north of 10°N in the Atlantic ECCO2 field, though with some differences. In particular, these jets nearly surface south of the Cape Verde Islands, likely due to the location of the Trade Wind Convergence Zone in the eastern Atlantic, further north than in the eastern Pacific; the several current cores at nearby latitudes in the eastern Atlantic (25°W) may actually be related to the presence of the Cape Verde Islands.

A major current is centered at 14°N, appearing as the most intense eastward flow within the CW stratum north of 5°N (Figure 13a). A southern branch is also discerned at 12°N, mostly within the uCW. Other

branches are detected north of the Cape Verde Islands flowing deeper than σ26.8 and centered at 18°N, and between the islands at 16°N. Since the Atlantic NEUC traditionally refers to the undercurrent at 4°N [*Stramma and Schott*, 1999], we refer to all these northern flows as the Cape Verde Current (CVC) System, with the southern (sCVC), central (CVC), and northern (nCVC) branches as shown in Figure 13.

6. Discussion and Conclusions

The analysis of a comprehensive *T/S* data set confirms the existence of a permanent abrupt thermohaline transition at σ26.8 (about 300 m depth) in the eastern tropical North Atlantic Ocean. The water mass analysis reveals the predominance of SACW in the uCW (σ26.3–σ26.8) and an abrupt increase in the contribution of NACW when entering the lCW (σ26.8–σ27.15). The maximum proportion of NACW (50%) is reached at the core of the naOMZ (at σ27.1), where minimal oxygen content is found. Such a markedly different water mass composition suggests that distinct circulation patterns rule the uCW and lCW, with a potentially important role of previously unreported water transfer from the well-ventilated northern subtropical gyre into the naOMZ core. In order to understand the development of these observational features, we have performed an analysis of the numerical Lagrangian trajectories, computed with the ECCO2 velocity field, that end up within the naOMZ.

The Lagrangian simulations reveal distinct pathways in the upper and lower CW layers (as clearly evidenced in the animation found in supporting information). In agreement with previous studies [*Stramma et al*., 2008b], the water mass supply within the uCW to the naOMZ is mainly (56%) carried by the nNECC and the northward branching of the NEUC, with a predominant contribution of southern origin particles. However, within the lCW these jets largely reduce their contribution in accordance with an enhancement of jets located further north, at the same time that the proportion of northern origin particles increases abruptly. In fact, more than two thirds of the total water supply within this layer occurs north of 10°N, mainly via an eastward flow centered at 14°N (29%) and other flows located further north (as much as 18°N) that are fed by waters recirculating from the northern subtropical gyre (30%). The existence of subsurface geostrophic eastward jets, north of 10°N and deeper than the westward flow of the subtropical gyre, has been recently pointed out for the North Pacific Ocean [*Qiu et al*., 2013a]. In the North Atlantic, repeated velocity observations along 23°W also reveal a predominant eastward flow centered at 14°N [*Brandt et al*., 2010]. North of the Cape Verde Islands, velocity observations are scarce to validate the existence of these jets. Nevertheless, we show that the high contribution of northern origin particles within these northern eastward flows, here referred as the Cape Verde Current System, accurately accounts for the increased proportion of NACW observed to occur in the lCW. Such a substantial northern supply within the lCW stratum presents a new perspective on the patterns of naOMZ ventilation.

In contrast with previous Eulerian studies, the Lagrangian description simultaneously incorporates the mean flow seasonal variability, the diapycnal fluxes and the mesoscale eddy field. Thus, a comparison of Lagrangian simulations of increased complexity allows isolating the contributions of the isopycnal fluxes, the diapycnal fluxes and the model subgrid-scale horizontal eddy diffusion in the water supply to the naOMZ, as briefly discussed next.

The distinct isopycnal circulation patterns of the uCW and lCW lead to the abrupt thermohaline transition at σ26.8, smoothed out by diapycnal fluxes through the interlayer exchange of particles. The diapycnal fluxes included in our Lagrangian experiments are based on meso and regional-scale diapycnal motions that appear to play a remarkable role in the renewal of the naOMZ thermocline. The regional diapycnal velocities have opposite prevailing signs within the two CW layers, affecting the water renewal rate of the naOMZ. In particular, for the sluggish lCW there is predominant downwelling along the trajectories, from shallower and faster to deeper and slower density levels, leading to a water supply enhancement of 20% solely due to the diapycnal transfer. This result points at the significant role that diapycnal fluxes play in the water renewal of the naOMZ.

Hahn et al. [2014] have shown, through the analysis of the meridional variability in the oxygen field, the relevance of meridional eddy stirring in the ventilation of the naOMZ. In our case, the nonfully eddy resolving ECCO2 field is unable to correctly reproduce the water mass composition of the naOMZ. Nevertheless, the addition of subgrid-scale diffusion leads to the accurate simulation of the observational hydrographic profiles. A major consequence of this added diffusion is the reduction of the water renewal times (by 25%)

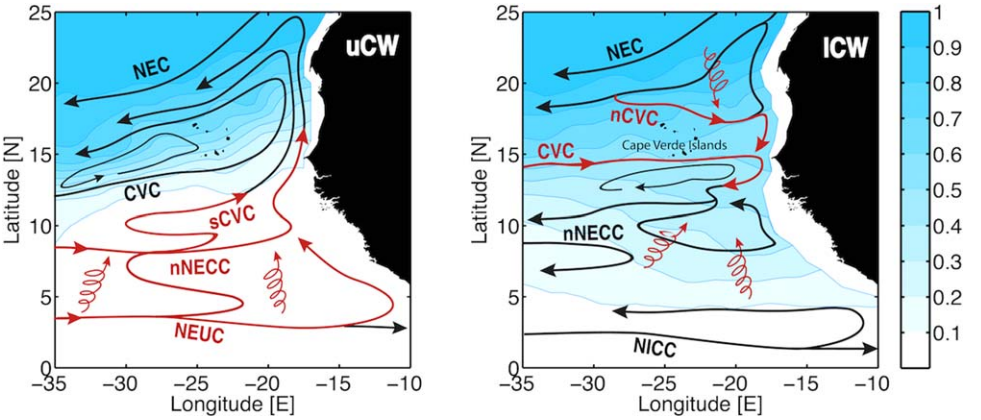

Figure 14. Schematics of the average circulation in the northeastern tropical Atlantic in the (left) uCW and (right) lCW layers. The distribution of the observed proportion of NACW is shown with blue contours. Major pathways to the naOMZ are highlighted in red. Twisted arrows represent regions where water mass renewal by eddy diffusion is enhanced.

due to an enhanced water transfer from the meridional boundaries of the naOMZ, i.e., the NEUC/nNECC region at the south and the subtropical gyre at the north.

The water mass pathways to the naOMZ, together with the main elements in its thermocline renewal, are sketched within the general circulation of the eastern tropical North Atlantic Ocean in Figure 14. The circulation in the uCW appears embedded within a broad cyclonic pattern, with the eastward NEUC and nNECC flows as the southern limb and the westward NEC as the northern arm. Previous studies have always related this scheme to the local, seasonal and shallow wind-driven Guinea Dome [*Stramma et al*., 2005, 2008b; *Karstensen et al*. 2008]. However, the relatively deep (reaching 300 m) vertical extent and much broader cyclonic circulation in the uCW, together with the horizontal distribution of the ECCO2 vertical velocities, suggest that the water supply in this layer is driven by the large-scale subtropical cell [*Zhang et al*., 2003; *Schott et al*., 2004].

The lCW circulation pattern is markedly different from that of the uCW. The lCW (1) is characterized by long residence times (3–4 times those in the uCW); (2) includes predominant eastward flows around the Cape Verde Islands and westward currents further south, sketching a broad anticyclonic circulation; and (3) presents an approximate antisymmetric horizontal distribution in the vertical velocities and layer thicknesses of both layers. These features have led us to hypothesize the existence of a lower subtropical cell within the lCW, with an inverse but weaker circulation scheme as compared with the uCW, analogous to the equatorial stacked tropical cells proposed by *Wang* [2005]. We suggest that both CW strata may interact through a normal baroclinic mode of circulation that leads to opposite circulation patterns.

Our results imply that the traditional constraint on OMZ ventilation from the subtropical gyre [*Luyten et al*., 1983] is limited, at least in the North Atlantic, to those layers above σ26.8, i.e., in the uCW stratum. In contrast, a weak but significant southward pathway from the subtropical North Atlantic to the naOMZ exists in the lCW. The existence of the proposed inverted cells emerges as a suggestive approach to the study of the world's OMZs. The substantial interannual and decadal variability of these cells [*Schott et al*., 2008] arises as a major cause for the changes in oxygen anomalies in the world OMZs during the last decades [*Deutsch et al*., 2011, 2014; *Ridder and England*, 2014].

Acknowledgments
This research has been funded by the Spanish Ministerio de Economía y Competitividad through projects MOC2 (CTM2008–06438-C02-01) and TIC-MOC (CTM2011–28867). J. Peña-Izquierdo has been supported through a FPI predoctoral grant linked to MOC2. E. van Sebille was supported by the Australian Research Council via grant DE130101336 and P. J. Llanillo was partly funded by CONICYT/FONDECYT de Postdoctorado through project 3150229. The authors acknowledge the NODC and Argo Program for making hydrographic data freely available (http://www.nodc.noaa.gov and http://www.coriolis.eu.org). We also thank the ECCO2/NASA program for providing the numerical assimilative simulation via their web page (http://ecco2.jpl.nasa.gov/products/). We would also like to sincerely thank our three reviewers for many useful comments and suggestions to an original version of this paper.

References

Banyte, D., T. Tanhua, M. Visbeck, D. W. R. Wallace, J. Karstensen, G. Krahmann, A. Schneider, L. Stramma, and M. Dengler (2012), Diapycnal diffusivity at the upper boundary of the tropical North Atlantic oxygen minimum zone, *J. Geophys. Res.*, *117*, C09016, doi:10.1029/2011JC007762.

Barton, E. (1989), The poleward undercurrent on the eastern boundary of the subtropical north atlantic, in *Coastal and Estuarine Studies*, edited by S. Neshyba, R. L. Smith, and C. N. K. Mooers, pp. 82–95, Springer, N. Y.

Blanke, B., M. Arhan, G. Madec, and S. Roche (1999), Warm water paths in the equatorial Atlantic as diagnosed with a general circulation model, *J. Phys. Oceanogr.*, *29*(11), 2753–2768.

Bopp, L., C. Le Que, M. Heimann, A. C. Manning, and P. Monfray (2002), Climate-induced oceanic oxygen fluxes : Implications for the contemporary carbon budget, *Global Biogeochem. Cycles*, *16*(2), 1022, doi:10.1029/2001GB001445.6-1-6-13.

Brandt, P., V. Hormann, A. Körtzinger, M. Visbeck, G. Krahmann, L. Stramma, R. Lumpkin, and C. Schmid (2010), Changes in the ventilation of the oxygen minimum zone of the tropical North Atlantic, *J. Phys. Oceanogr.*, *40*(8), 1784–1801, doi:10.1175/2010JPO4301.1.

Brandt, P., et al. (2014), On the role of circulation and mixing in the ventilation of oxygen minimum zones with a focus on the eastern tropical North Atlantic, *Biogeosci. Discuss.*, *11*(8), 12,069–12,136, doi:10.5194/bgd-11-12069-2014.
Deutsch, C., H. Brix, T. Ito, H. Frenzel, and L. Thompson (2011), Climate-forced variability of ocean hypoxia, *Science*, *333*(6040), 336–339, doi:10.1126/science.1202422.
Deutsch, C., et al. (2014), Centennial changes in North Pacific anoxia linked to tropical trade winds, *Science*, *345*, 665–668, doi:10.1126/science.1252332.
Döös, K., J. Nycander, and A. C. Coward (2008), Lagrangian decomposition of the Deacon Cell, *J. Geophys. Res.*, *113*, C07028, doi:10.1029/2007JC004351.
Döös, K., V. Rupolo, and L. Brodeau (2011), Dispersion of surface drifters and model-simulated trajectories, *Ocean Modell.*, *39*(3–4), 301–310, doi:10.1016/j.ocemod.2011.05.005.
Duteil, O., F. U. Schwarzkopf, C. W. Böning, and A. Oschlies (2014), Major role of the equatorial current system in setting oxygen levels in the eastern tropical Atlantic Ocean: A high-resolution model study, *Geophys. Res. Lett.*, *41*, 2033–2040, doi:10.1002/2013GL058888.
Elmoussaoui, A., M. Arhan, and A. M. Treguier (2005), Model-inferred upper ocean circulation in the eastern tropics of the North Atlantic, *Deep Sea Res., Part I*, *52*(7), 1093–1120, doi:10.1016/j.dsr.2005.01.010.
Fischer, T., D. Banyte, P. Brandt, M. Dengler, G. Krahmann, T. Tanhua, and M. Visbeck (2013), Diapycnal oxygen supply to the tropical North Atlantic oxygen minimum zone, *Biogeosciences*, *10*(7), 5079–5093, doi:10.5194/bg-10-5079-2013.
Fraga, F. (1974), Distribution des masses d'eau dans l'upwelling de mauritanie, *Tethysethys*, *6*, 5–10.
Fratantoni, D. M., W. E. Johns, T. L. Townsend, and H. E. Hurlburt (2000), Low-latitude circulation and mass transport pathways in a model of the tropical Atlantic Ocean, *J. Phys. Oceanogr.*, *30*, 1944–1966.
Fu, L.-L. (2009), Pattern and velocity of propagation of the global ocean eddy variability, *J. Geophys. Res.*, *114*, C11017, doi:10.1029/2009JC005349.
Garcia, H., A. Cruzado, L. Gordon, and J. Escanez (1998), Decadal-scale chemical variability in the subtropical North Atlantic deduced from nutrient and oxygen data, *J. Geophys. Res.*, *103*(C2), 2817–2830, doi:10.1029/97JC03037.
Gnanadesikan, A., J. L. Russell, F. Zeng, and G. Fluid (2007), How does ocean ventilation change under global warming, *Ocean Sci.*, *3*, 43–53.
Gouretski, V., and P. Koltermann (2004), WOCE global hydrographic climatology: A technical report, Berichte des Bundesamtes für Seeschifffahrt und Hydrographie, 35.
Griffies, S. M., R. C. Pacanowski, and R. W. Hallberg (2000), Spurious diapycnal mixing associated with advection in a z-coordinate ocean model, *Mon. Weather Rev.*, *128*, 538–564.
Hahn, J., P. Brandt, R. J. Greatbatch, G. Krahmann, and A. Körtzinger (2014), Oxygen variance and meridional oxygen supply in the Tropical North East Atlantic oxygen minimum zone, *Clim. Dyn.*, *43*, 2999–3024, doi:10.1007/s00382-014-2065-0.
Hazeleger, W., and S. Drijfhout (2006), Subtropical cells and meridional overturning circulation pathways in the tropical Atlantic, *J. Geophys. Res.*, *111*, C03013, doi:10.1029/2005JC002942.
Joos, F., G.-K. Plattner, T. F. Stocker, A. Körtzinger, and D. W. R. Wallace (2003), Trends in marine dissolved oxygen: Implications for ocean circulation changes and the carbon budget, *Eos Trans. AGU*, *84*(21), 197–201, doi:10.1029/2003EO210001.
Karstensen, J., L. Stramma, and M. Visbeck (2008), Oxygen minimum zones in the eastern tropical Atlantic and Pacific oceans, *Prog. Oceanogr.*, *77*(4), 331–350, doi:10.1016/j.pocean.2007.05.009.
Kirchner, K., M. Rhein, S. Hüttl-Kabus, and C. W. Böning (2009), On the spreading of South Atlantic Water into the Northern Hemisphere, *J. Geophys. Res.*, *114*, C05019, doi:10.1029/2008JC005165.
Lam, P., and M. M. M. Kuypers (2011), Microbial nitrogen cycling processes in oxygen minimum zones, *Annu. Rev. Mar. Sci.*, *3*(1), 317–345, doi:10.1146/annurev-marine-120709-142814.
Lázaro, C., M. J. Fernandes, A. M. P. Santos, and P. Oliveira (2005), Seasonal and interannual variability of surface circulation in the Cape Verde region from 8 years of merged T/P and ERS-2 altimeter data, *Remote Sens. Environ.*, *98*(1), 45–62, doi:10.1016/j.rse.2005.06.005.
Lu, P., J. P. McCreary, and B. A. Klinger (1998), Meridional circulation cells and the source waters of the Pacific Equatorial Undercurrent, *J. Phys. Oceanogr.*, *28*, 62–84.
Luyten, J. R., J. Pedlosky, and H. Stommel (1983), The ventilated thermocline, *J. Phys. Oceanogr.*, *13*, 292–309, doi:10.1175/1520-0485(1983)013<0292:TVT>2.0.CO;2.
Mackas, D. L., K. L. Denman, and A. F. Bennett (1987), Least squares multiple tracer analysis of water mass composition, *J. Geophys. Res.*, *92*(C3), 2907–2918, doi:10.1029/JC092iC03p02907.
Marshall, J., A. Adcroft, C. Hill, L. Perelman, and C. Heisey (1997), A finite-volume, incompressible Navier Stokes model for studies of the ocean on parallel computers, *J. Geophys. Res.*, *102*(C3), 5753–5766, doi:10.1029/96JC02775.
Matear, R. J., and A. C. Hirst (2003), Long-term changes in dissolved oxygen concentrations in the ocean caused by protracted global warming, *Global Biogeochem. Cycles*, *17*(4), 1125, doi:10.1029/2002GB001997.
Millero, F. J., R. Feistel, D. G. Wright, and T. J. McDougall (2008), The composition of standard seawater and the definition of the reference-composition salinity scale, *Deep Sea Res., Part I*, *55*(1), 50–72.
Mittelstaedt, E. (1991), The ocean boundary along the northwest African coast: Circulation and oceanographic properties at the sea surface, *Prog. Oceanogr.*, *26*(4), 307–355.
Oschlies, A., K. G. Schulz, U. Riebesell, and A. Schmittner (2008), Simulated 21st century's increase in oceanic suboxia by CO_2—Enhanced biotic carbon export, *Global Biogeochem. Cycles*, *22*, GB4008, doi:10.1029/2007GB003147.
Paris, C. B., J. Helgers, E. van Sebille, and A. Srinivasan (2013), Connectivity modeling system: A probabilistic modeling tool for the multi-scale tracking of biotic and abiotic variability in the ocean, *Environ. Model. Software*, *42*, 47–54, doi:10.1016/j.envsoft.2012.12.006.
Pastor, M. V., J. Peña-Izquierdo, J. L. Pelegrí, and Á. Marrero-Díaz (2012), Meridional changes in water mass distributions off NW Africa during November 2007/2008, *Ciencias Mar.*, *38*, 223–244.
Paulmier, A., D. Ruiz-Pino, and V. Garçon (2011), CO_2 maximum in the oxygen minimum zone (OMZ), *Biogeosciences*, *8*(2), 239–252, doi:10.5194/bg-8-239-2011.
Peña-Izquierdo, J., J. L. Pelegrí, M. V. Pastor, P. Castellanos, M. Emelianov, M. Gasser, J. Salvador, and E. Vázquez-Domínguez (2012), The continental slope current system between Cape Verde and the Canary Islands, *Sci. Mar.*, *76*(S1), 65–78, doi:10.3989/scimar.03607.18C.
Poole, R., and M. Tomczak (1999), Optimum multiparameter analysis of the water mass structure in the Atlantic Ocean thermocline, *Deep Sea Res., Part I*, *46*(11), 1895–1921, doi:10.1016/S0967-0637(99)00025-4.
Qiu, B., D. L. Rudnick, S. Chen, and Y. Kashino (2013a), Quasi-stationary North Equatorial Undercurrent jets across the tropical North Pacific Ocean, *Geophys. Res. Lett.*, *40*, 2183–2187, doi:10.1002/grl.50394.
Qiu, B., S. Chen, and H. Sasaki (2013b), Generation of the North Equatorial Undercurrent Jets by Triad Baroclinic Rossby wave interactions, *J. Phys. Oceanogr.*, *43*(12), 2682–2698, doi:10.1175/JPO-D-13-099.1.

Reid, J. L. (1994), On the total geostrophic circulation of the North Atlantic Ocean: Flow patterns, tracers, and transports, *Prog. Oceanogr.*, *33*(1), 1–92, doi:10.1016/0079-6611(94)90014-0.
Rhein, M., K. Kirchner, C. Mertens, R. Steinfeldt, M. Walter, and U. Fleischmann-Wischnath (2005), Transport of South Atlantic water through the passages south of Guadeloupe and across 16°N, 2000–2004, *Deep Sea Res., Part I*, *52*(12), 2234–2249, doi:10.1016/j.dsr.2005.08.003.
Ridder, N. N., and M. H. England (2014), Sensitivity of ocean oxygenation to variations in tropical zonal wind stress magnitude, *Global Biogeochem. Cycles*, *28*, 909–926, doi:10.1002/2013GB004708.
Schott, F. A., J. P. Mccreary, and G. C. Johnson (2004), Shallow Overturning Circulations of the tropical-subtropical oceans, in *Earth's Climate: The Ocean-Atmosphere Interaction, Geophys. Monogr. Ser.*, vol. 147, edited by C. Wang, S.-P. Xie, and J. A. Carton, pp. 261–304, AGU, Washington, D. C.
Schott, F. A., L. Stramma, W. Wang, B. S. Giese, and R. Zantopp (2008), Pacific Subtropical Cell variability in the SODA 2.0.2/3 assimilation, *Geophys. Res. Lett.*, *35*, L10607, doi:10.1029/2008GL033757.
Siedler, G., N. Zangenberg, and R. Onken (1992), Seasonal changes in the tropical Atlantic Circulation: Observation and simulation of the Guinea Dome, *J. Geophys. Res.*, *97*(C1), 703–715.
Stramma, L., and F. Schott (1999), The mean flow field of the tropical Atlantic Ocean, *Deep Sea Res., Part II*, *46*(1–2), 279–303, doi:10.1016/S0967-0645(98)00109-X.
Stramma, L., S. Hüttl, and J. Schafstall (2005), Water masses and currents in the upper tropical northeast Atlantic off northwest Africa, *J. Geophys. Res.*, *110*, C12006, doi:10.1029/2005JC002939.
Stramma, L., G. C. Johnson, J. Sprintall, and V. Mohrholz (2008a), Expanding oxygen-minimum zones in the tropical oceans, *Science*, *320*(5876), 655–658, doi:10.1126/science.1153847.
Stramma, L., P. Brandt, J. Schafstall, F. Schott, J. Fischer, and A. Körtzinger (2008b), Oxygen minimum zone in the North Atlantic south and east of the Cape Verde Islands, *J. Geophys. Res.*, *113*, C04014, doi:10.1029/2007JC004369.
Stramma, L., M. Visbeck, P. Brandt, T. Tanhua, and D. Wallace (2009), Deoxygenation in the oxygen minimum zone of the eastern tropical North Atlantic, *Geophys. Res. Lett.*, *36*, L20607, doi:10.1029/2009GL039593.
Tomczak, M. (1981), An analysis of mixing in the frontal zone of South and North Atlantic Central Water off North-West Africa, *Prog. Oceanogr.*, *10*, 173–192.
Tomczak, M., and D. G. B. Large (1989), Multiparameter analysis of mixing in the thermocline represent of the Eastern Indian Ocean, *J. Geophys. Res.*, *94*(C11), 16,141–16,149.
Van Sebille, E., W. E. Johns, and L. M. Beal (2012), Does the vorticity flux from Agulhas rings control the zonal pathway of NADW across the South Atlantic?, *J. Geophys. Res.*, *117*, C05037, doi:10.1029/2011JC007684.
Van Sebille, E., P. Spence, M. R. Mazloff, M. H. England, S. R. Rintoul, and O. A. Saenko (2013), Abyssal connections of Antarctic Bottom Water in a Southern Ocean State Estimate, *Geophys. Res. Lett.*, *40*, 2177–2182, doi:10.1002/grl.50483.
Vaquer-Sunyer, R., and C. Duarte (2008), Thresholds of hypoxia for marine biodiversity, *Proc. Natl. Acad. Sci. U. S. A.*, *105*(40), 15,452–15,457.
Voituriez, B., and R. Chuchla (1978), Influence of the Southern Atlantic Central Water on the distribution of salinity and oxygen in the northeast tropical Atlantic Ocean, *Deep Sea Res.*, *25*, 107–117.
Wang, C. (2005), Subthermocline tropical cells and equatorial subsurface countercurrents, *Deep Sea Res., Part I*, *52*(1), 123–135, doi:10.1016/j.dsr.2004.08.009.
Xuang, R. X. (2010), *Ocean Circulation, Wind-Driven and Thermohaline Processes*, section 4.1, 261–350, Cambridge Univ. Press, N. Y.
Zhang, D., M. J. McPhaden, and W. E. Johns (2003), Observational evidence for flow between the subtropical and tropical Atlantic : The Atlantic subtropical cells, *J. Phys. Oceanogr.*, *33*, 1783–1797.
Zenk, W., B. Klein, and M. Schröder (1991), Cape Verde frontal zone, *Deep Sea Res.*, *38*, suppl. 1, S505–S530.